Spin Wave Resonance and Relaxation in Microwave Magnetic Multilayer Structures and Devices

by

Cheng Wu

A dissertation submitted to the graduate faculty in Physics in partial fulfillment of the

Requirements for the Degree of Doctor of Philosophy,

Department of Physics and Astronomy, City University of New York

2008

This manuscript has been read and accepted for the
Graduate Faculty in Physics in satisfaction of the
dissertation requirement for the degree of Doctor of Philosophy.

Dr. Yuhang Ren

Date
Chair of Examining Committee

Dr. Steven G. Greenbaum

Date
Executive Officer

Dr. Ying-Chih Chen

Dr. Jiufeng Tu

Dr. Godfrey Gumbs

Dr. Kai Shum

Supervision Committee

THE CITY UNIVERSITY OF NEW YORK

Abstract

Spin Wave Resonance and Relaxation in Microwave Magnetic Multilayer Structures and Devices

by

Cheng Wu

Adviser: Professor Yuhang Ren

The continuous and increasing demand for higher frequency magnetic microwave structures triggered a tremendous development in the field of magnetization dynamics over the past decade. In order to develop smaller and faster devices, more efforts are required to achieve a better understanding of the complex magnetization precessional dynamics, the magnetization anisotropy, and the sources of spin scattering at the nanoscale.

This thesis presents measurements of magnetic precession and relaxation dynamics in multilayer ferromagnetic films of CoFe/PtMn/CoFe in both frequency and time domain. First, we conducted the ferromagnetic resonance (FMR) measurements for samples with the ferromagnetic CoFe layer thicknesses varying from 10 Å to 500 Å. The magnetic anisotropic parameters were determined by rotating the field aligned axis with respect to the spectral field in the configurations of both in-plane and out-of-plane. Moreover, we identified a high-order standing spin wave in our spectra and found a "critical angle" in the multilayer samples. We included an effective surface anisotropy field to describe our results. This allows us to determine the exchange interaction stiffness in the CoFe layers. Next, we performed pump-probe Magneto-Optical Kerr Effect experiments in the multilayer films. Three precession modes were observed in the Voigt geometry. The modes are assigned to the exchange-dominated spin wave excitations and the non-homogeneous dipole mode. We developed a comprehensive model of the magnetic eigenmodes and their coupling to light to gain accurate values of the exchange, bulk and surface anisotropy constants. The results are consistent with those from the FMR measurements. Finally, the measured resonance linewidths of CoFe/PtMn/CoFe films were analyzed by the thickness dependence of the CoFe layers. We discussed the contribution of the Gilbert damping, two magnon scattering, as well as surface and interface to the FMR linewidth and concluded the two magnon scattering plays the most important role in FMR linewidth broadening and reaffirmed the significance of surface effects for spin wave damping in these samples.

The results of this thesis will lead to new insights into important magnetic properties of ferromagnetic films and therefore provide essential knowledge for optimizing the GHz response of the nanoscale magnetic elements and devices.

Acknowledgements

First of all, I would like to thank my advisor, Prof. Yuhang Ren, for the excellent advice and mentoring throughout my Ph.D. study at Hunter College of City University of New York. I am greatly indebted to his continuous help in almost every way from my very first day of working in his lab. He instructed me step by step in every aspect from the most fundamental physics concepts to the advanced experimental setups. He encouraged me when I was depressed and exhausted and taught me not only physics, but also critical thinking which is essential for scientific research. I was fortunate to have been working with him with such extensive knowledge in both experimental and theoretical condensed matter physics and such great enthusiasm for research and experiments. His incisive comments and inspirational ideas always bring a fresh perspective to my research project. I could not have come to this point without his encouragement and guidance.

I am very grateful to Prof. Steve Greenbaum and a lot of people from his lab, especially Dr. Phil Stallworth and Dr. Amish Khalfan. I conducted the ferromagnetic resoance measurements in their NMR/EPR lab and learned a lot from equipment setup to experimental techniques.

Next, I would like to thank Prof. N. X. Sun of Northeastern University, Prof. H. Zhen of University at Buffalo SUNY and Prof. Q. Li of Pennsylvania State University for their state-of-the-art samples.

I also would like to thank Prof. Ying-Chih Chen, Prof. Jiufeng Tu, Prof. Godfrey Gumbs, and Prof. Kai Sun for their kindness to serve on my defense committee. In our group, I have been working closely with Tetiana Nosach, Mark Ebrahim and Yu Gong. All of them have made big contributions to the measurements and analysis of the material described in my thesis. I benefited a lot from their valuable comments and suggestions on this thesis.

Finally, I would like to express my deepest appreciation to my family. For many years, my wife Cuihua He continuously support me in my pursuit of physics research, her endless love and sacrifice undoubtedly inspired me to work hard. My parents Runshan Wu and Yimin Zhang encouraged me to persist and took care of my daughter for such a long time. I also deeply appreciate my parents-in-law Jiliang He and Yanling Lai who offered babysitting in our years of hardship, and my sister Xingchi Wu, who gave me precious suggestions from time to time.

Contents

List of Figures

Chapter 1

Introduction

1.1 Microwave Magnetic Materials and Devices

Over the past 20 years, physicists have developed techniques that allow them to deposit sequential layers of atoms in regular crystalline planes on a surface in a controlled way. The technology advances thus made the fabrication of magnetic thin film at nanoscale feasible. By alternating layers of different magnetic properties, one can explore how magnetic ordering (the precise arrangement of the electron spins in the layers) propagates across the layers.

Thin film magnetic materials find immediate application within the magnetic data storage industry although other opportunities exist for the use of thin film magnetic materials within communications technology. However, the soft magnetic materials integrated in high frequency devices must be characterized by high saturation magnetization, controllable uniaxial anisotropy and process compatibility; this is believed to be difficult to combine with conventional single alloy materials [1]. To overcome this limitation, Y Lamy and B. Viala proposed a different route where the contributions $4\pi M_S$ and H_K to the f_{FMR} can be optimized independently by using two separate materials: ferromagnetic/antiferromagnetic [2,3]. In recent years, research about different composition of multilayer ferromagnetic thin films has been extensively carried out and a comprehensive understanding of the magnetic prosperities of FM/AFM bilayer, AFM/FM/AFM and FM/AFM/FM trilayers is promising [4, 5].

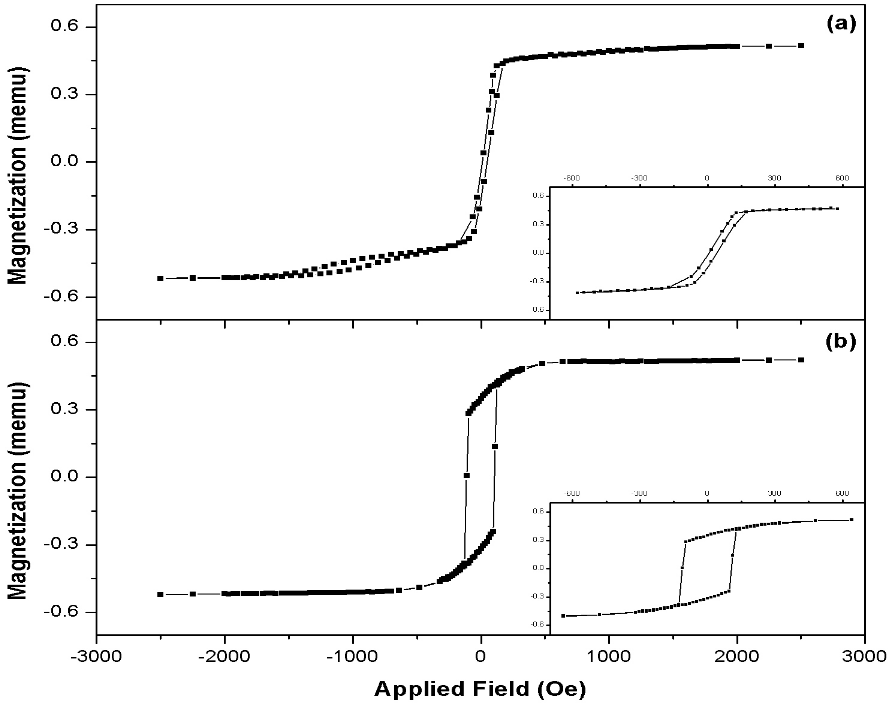

Fig. 1.1 As the result of the interfacial interaction and/or the exchange coupling, (a) sandwiched AFM/FM/AFM films show excellent magnetic softness with low coercivity compared with (b) single layer thin film

In the application of magnetic material, Eddy current is one of the most significant dissipation mechanisms, by which the excitation is eventually transferred into heat. Y. Lamy and B. Viala has shown that magnetic/nonmagnetic multilayers are effective in suppressing eddy currents and display excellent soft magnetic properties with coercivity reduced by orders of magnitude. Both FM/AFM bilayer and AFM/FM/AFM trilayer demonstrate the combination of very high $4\pi M_S$ and ultra large H_K.

Soft magnetic thin films with high saturation magnetization typically have quite limited anisotropy fields, which severely restrict their applications at RF/microwave frequencies [6]. A unidirectional anisotropy field can be achieved in exchange biased ferromagnetic (FM)/antiferrromagnetic (AFM) composite materials as a result of an interfacial interaction or exchange coupling, which can be used to boost the effective anisotropy field of high saturation magnetization materials [7,8]. Exchange-coupled AFM/FM bilayers [9–13], and FM/AFM/FM trilayers [14] exhibit enhanced anisotropy fields due to exchange coupling. Because of the properties, the multilayer structures are promising for applications in micro-sensor and high-frequency devices. such as magnetic band stop filters [15,16] and magnetic integrated inductors [17,18]. Moreover, the high saturation magnetization and low-temperature processing technologies of the structures are compatible to the silicon integrated circuits and monolithic microwave integrated circuits (MMIC) process technologies.

In our research, we studied magnetic dynamical properties including magnetic anisotropy, interlayer coupling and magnetic damping in the advanced FM/AFM/FM thin films which were fabricated by our collaborators at Northeastern University. Compared to the AFM/FM/AFM trilayers and FM/AFM bilayers, trilayers of FM/AFM/FM have their advantages for many microwave applications. First, trilayers of FM/AFM/FM have a higher effective magnetization M_{eff}, which can be expressed as:

$$M_{eff} = \Sigma t_{FM} M_s / (\Sigma t_{FM} + \Sigma t_{NM}) . \qquad (1)$$

Here M_s and t_{FM} are the saturation magnetization and thickness of the magnetic layers and t_{NM} is the nonmagnetic layer thickness, such as AFM layer, etc., and therefore, a higher flux conduction capability. Second, FM/AFM/FM trilayer leads to lower coercivity compared to the bilayers of AFM/FM, which was possibly due to magnetic charge compensation at the magnetic film edges [19].

The investigations are expected to answer some important questions: What is the dependence of anisotropy field distribution on thicknesses of the FM layers and the AFM layer? How does the magnetization precession and magnetic switching differ for the different structure configurations? How do the surface and interfaces affect the magnetization responses?

The ongoing studies of multilayered magnetic materials are making it more apparent that the knowledge of their dynamical magnetic excitation process will play a decisive role in understanding fundamental magnetic interactions and potential application of those materials [20]. The very interest in investigating the multilayer ferromagnetic thin films is now related to the dynamical magnetic excitation and relaxation of the samples. However, investigations of magnetization dynamics were far from complete and there are still fundamental questions regarding collective spin excitations and surface/interface effect in these systems [21-24]. In particular, experimental data on collective magnetic excitations and spin relaxations, affected by interlayer coupling and surface/interface effects, are scarce.

As collective spin excitations and relaxation dynamics appear to play an essential role in the magnetic properties of the multilayer film devices, a detailed investigation of the surface (and interface) magnetism and spin coherence is needed. The understanding of the fundamental dynamical magnetic excitations - which is intimately connected with the exchange interaction between different layers – has become the essential part of our research subject. By conducting experiments of these multilayer thin using microwave FMR and pump-probe ultrafast laser techniques, we have gotten interesting results and our analysis has proven the validity of our theoretical model.

1.2 Magnetization Excitation

When a magnetic field is applied to magnetic material, the magnetization of the material will align with the applied field. How does magnetization behave in this process? What controls the rate of magnetization change? Magnetization dynamics study this process and answer these questions.

At equilibrium, the direction of magnetization M_s in ferromagnetic material is always aligned to that of the effective field H_{eff} applied to the material. If H_{eff} suddenly changes its direction, there will be a torque τ acting on M_s,

$$\tau = M_s \times H_{eff} \tag{2}$$

which will cause the change of angular momentum L,

$$\frac{dL}{dt} = \tau$$

Because

$$M_s = -\gamma L\,,$$

Then we have,

$$\frac{dM_s}{dt} = -\gamma\tau = -\gamma M_s \times H_{eff} \tag{3}$$

in which $\gamma = g\dfrac{e}{2m_e}$ is the gyromagnetic ratio and g is the spectroscopic splitting factor. With τ acting on M_s, M_s will precess around the axis of H_{eff}. The process is called Larmor precession.

From an analogy in classical mechanics, we know the magnetization will precess around the effective field forever if there is no damping at all. However, in reality this will never happen because damping always exist in any ferromagnetic material, causing the energy of precession dissipated. The precession frequency will be less than Larmor frequency and the magnetization will precess spirally and end up with aligning with the effective field. The equation of motion describing magnetization precession with damping is the well-known Landau-Lifshitz-Gilbert equation [25]:

$$\frac{dM_s}{dt} = -\gamma M_s \times H_{eff} + \frac{\alpha}{M_s}(M_s \times \frac{dM_s}{dt}) \qquad (4)$$

where α is the damping constant with no dimension. The first term describes the precession of the magnetization under the influence of the applied field, while the second describes how the magnetization vector spirals in towards the field direction as time progresses.

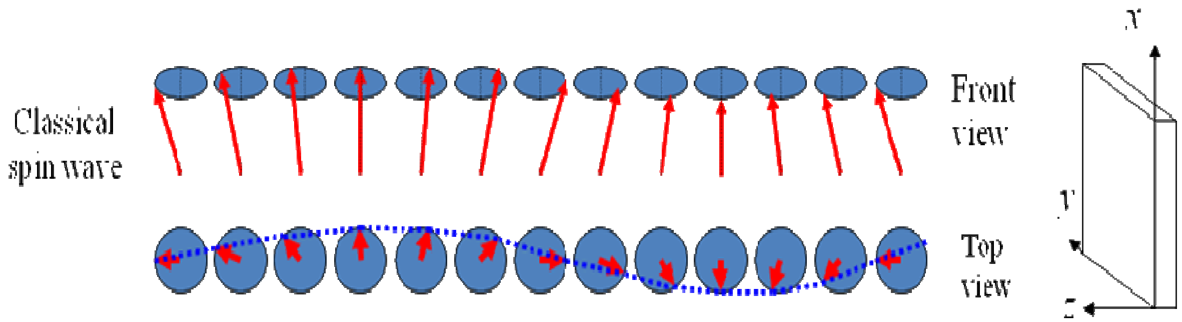

Fig. 1.2 Classical spin wave propagation

The magnetization vector in ferromagnetic material aligns with the effective field until it is disturbed from the equilibrium direction, then it will precess around the equilibrium direction spirally and finally tend to align with effective field. All the spins will precess in the same frequency, if the phases of neighboring spins are not the same, we will see the propagation of magnetic excitation, which is called spin wave. If the individual moments, or "spins" precess at the same phase, it is commonly referred to as the uniform mode of spin wave.

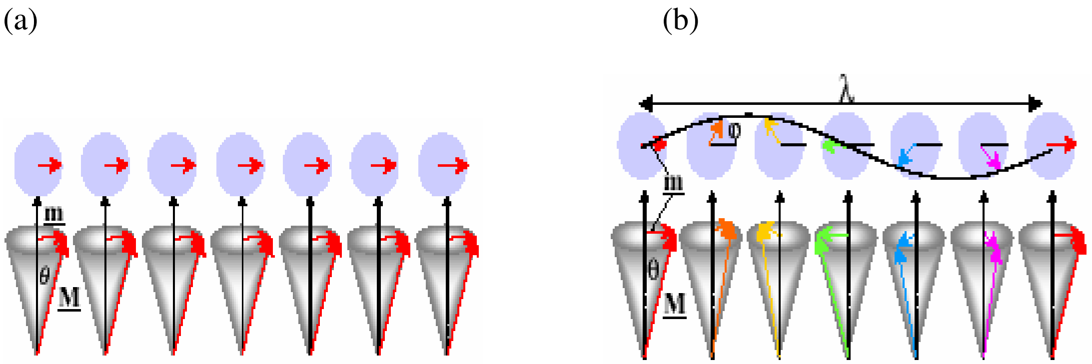

Fig. 1.3: (a) Uniform Mode (b) Standing Wave Mode (note here we assume the surface spins completely pinned.)

As temperature increases, the thermal excitation of spin waves reduces the spontaneous magnetization of a ferromagnet. The energies of spin waves are typically only μeV in keeping with typical Curie points at room temperature and below. Spin waves exist in magnetic systems and refer to the collective precession of magnetic moments around the easy axis direction. The precession is due to the torque caused by an effective magnetic field, which includes the contributions of bulk anisotropies, external magnetic fields, and exchange interactions in thin films, or interlayer couplings in superlattices. Investigation on propagations of magnetic excitation in ferromagnetic thin films can tell us essential information about surface anisotropy and interface effects which could be crucial in the development of magnetic devices.

The spin wave excitations provide powerful means for studying the dynamic properties of magnetic media in general and those of laterally patterned magnetic structures in particular. From spin wave measurements basic information on the magnetic properties, such as magnetic anisotropy contributions, the homogeneity of the internal field, as well as coupling between magnetic elements can be extracted. This information is often hard to obtain by other methods.

Magnetization dynamics in films could be investigated through four experimental methods: inelastic neutron scattering, inelastic light scattering (Brillouin scattering, Raman scattering and inelastic X-ray scattering) [26], inelastic electron scattering (spin-resolved electron energy loss spectroscopy) and spin-wave resonance, also known as ferromagnetic resonance (FMR) [27,28]. In the first method the energy loss of a beam of neutrons that excites a magnon is measured, typically as a function of scattering vector (or equivalently momentum transfer), temperature and external magnetic field. Inelastic neutron scattering measurements can determine the dispersion curve for magnons just as they can for phonons. Ferromagnetic (or antiferromagnetic) resonance instead measures the absorption of microwaves, incident on a magnetic material, by spin waves, typically as a function of angle, temperature and applied field. Brillouin scattering similarly measures the energy loss of photons (usually at a convenient visible wavelength) reflected from or transmitted through a magnetic material. Brillouin spectroscopy is similar to the more widely known Raman scattering but probes a lower energy and has a higher energy resolution in order to be able to detect the meV energy of magnons.

1.3 Ferromagnetic Resonance Techniques

One important technique for investigating magnetic dynamics in frequency domain is ferromagnetic resonance (FMR). In our lab, we used FMR to explore magnetic properties of the multilayer ferromagnetic thin film samples.

FMR was discovered by V. K. Arkad'yev when he observed the absorption of UHF radiation by ferromagnetic materials in 1911 [29]. A qualitative explanation of FMR along with an explanation of the results from Arkad'yev was offered up by Ya. G. Dorfman in 1923 [30]. The experimental ferromagnetic resonance (FMR) was introduced by J. H. E. Griffiths in 1946 [31]. Since then FMR has been a standard technique for studying the ground-state properties of magnetic materials, especially for the investigation of magnetic anisotropy. In the past ten years, the magnetic anisotropy, interlayer exchange coupling and the relaxation of magnetization of ultrathin films and superlattices have been extensively studied by FMR.

The amount of microwave radiation absorbed by the sample is monitored using a microwave detector. The values of magnetic field strength which give rise to absorption of the microwave radiation are indicative of the structure of the sample being tested. In known ferromagnetic resonance measurements, a sample of a material to be tested is located within a resonant cavity, the resonance of the cavity being selected for the frequency of microwave radiation that is to be directed at the sample. The resonant cavity enhances the signal to noise ratio of the ferromagnetic resonance measurement [32].

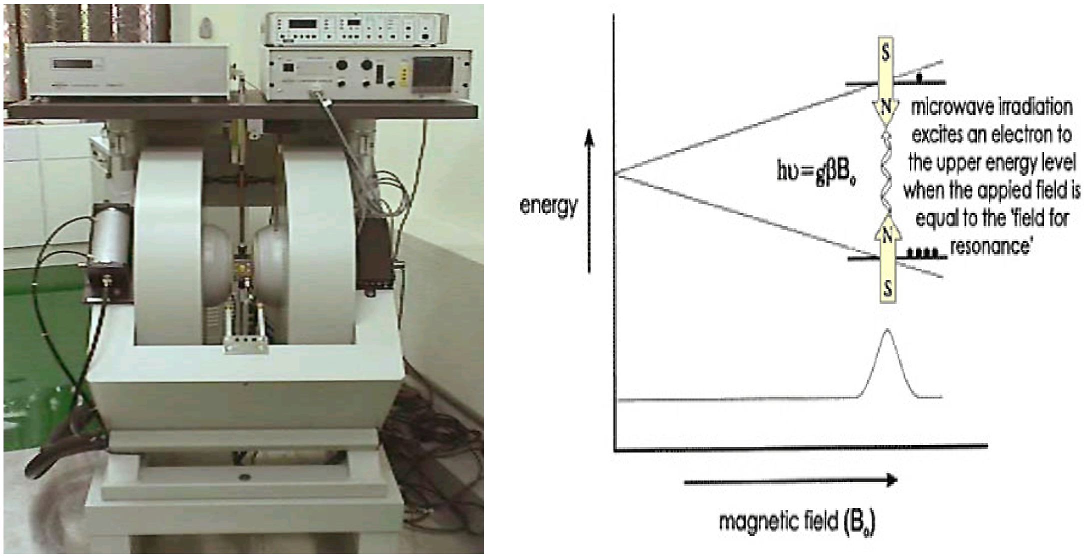

Fig. 1.4: FMR facility: Bruker EMX Series X-band EPR spectrometer

In FMR measurements, the resonance field H_{eff} provides us the direct magnetization information about the sample. This method allows us to measure the gyromagnetic ratio γ, the Gilbert damping parameter α, the exchange constant A and the anisotropy constant K.

Ferromagnetic resonance is a convenient laboratory method for determining the effect of magnetocrystalline anisotropy on the dispersion of spin waves. The ferromagnetic resonance absorption is similar to the nuclear resonance absorption with the difference being that FMR probes the magnetic moment of electrons instead of the nucleus. FMR allows us to observe the dynamic phenomena like exchange-bias interactions, coupled oscillations, domain and domain wall resonance etc. We can also investigate the material transitions at low temperatures if we use the cavity with a cryostat.

1.4 Time-resolved Optical Magneto-optical Kerr Measurement

Another important technique for studying magnetization dynamics is the time-resolved magneto-optical Kerr effect (MOKE) spectroscopy. The combined pico-second temporal and sub-micrometer spatial resolutions allow one to directly study the time dependence of magnetic excitations and acquire "snapshot" magnetic maps of the sample surface [33]. The observed non-uniform spatial problems are not easily expected from electrical measurements.

The plane of polarization of the light can slightly rotate when a beam of polarized light reflects off a magnetized surface,. This phenomenon is known as the magneto-optic Kerr effect, named after Reverend Kerr who discovered the effect in the 19th Century [34]. In fact the strength of the magnetization of the material affects the change in the polarization of the light which is reflected on the surface of a magnetic thin film. The technique is sometimes referred to as SMOKE, where the S stands for surface. However, the light is known to penetrate about 20 nm into the surface for most metals which means that MOKE is not particularly surface sensitive.

MOKE can be further categorized by the direction of the magnetization vector with respect to the reflecting surface and the plane of incidence.

(1) Polar MOKE: When the magnetic field H is applied normal to the film plane and parallel to the plane of incidence, the effect is called the polar Kerr effect. Thus it is sensitive to the perpendicular component of the magnetization. To simplify the analysis,

near normal incidence is usually employed when doing experiments in the polar geometry. The polar signal is typically an order of magnitude larger than the longitudinal signal because of different optical prefactors.

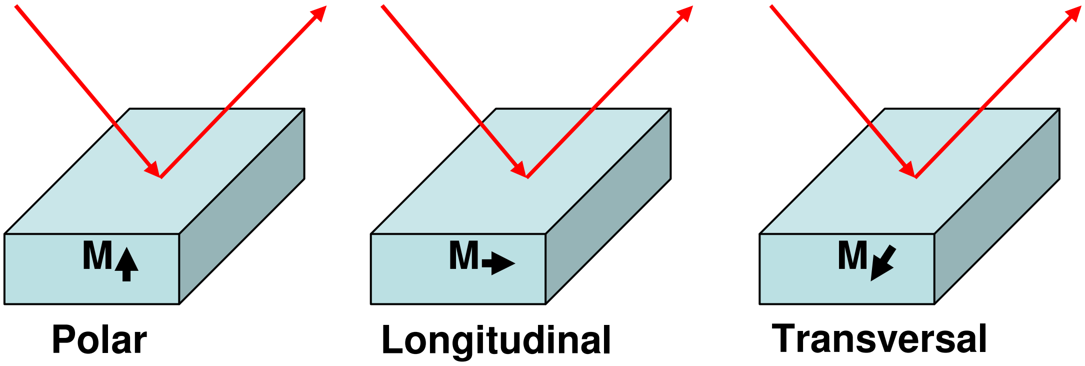

Fig. 1.5 Category of MOKE

(2) Longitudinal MOKE: In the longitudinal effect, the magnetization vector H is applied in the film plane and in the plane of the incident light, making it sensitive to the in-plane component of the magnetization. Just like in polar MOKE, linearly polarized light incident on the surface becomes elliptically polarized, with the change in polarization directly proportional to the component of magnetization that is parallel to the reflection surface and parallel to the plane of incidence.

(3) Transversal MOKE: When the magnetization H is applied in the film plane, but perpendicular to the incident plane of the light, it is said to be in the transverse configuration. This change in reflectivity is proportional to the component of magnetization that is perpendicular to the plane of incidence and parallel to the surface.

In addition to the polar, longitudinal and transverse Kerr effects which depend linear on the respective magnetization components, there are also higher order quadratic effects, for which the Kerr angle depends on product terms involving the polar, longitudinal and transverse magnetization components. We will not discuss that in details in this thesis. MOKE can be incorporated into microscopes so that magnetic domain imaging becomes possible. The more traditional optical microscopes can be used in this manner, or the more recent near-field microscopes.

1.5 Outline of the dissertation

In chapter 1, we discuss the importance of ferromagnetic multilayer thin films, the fundamental dynamic magnetic excitation in the thin films and the experimental methods used to investigate magnetic properties in those thin films.

In chapter 2, we give a theoretical description of the spin wave dynamics specifically for the trilayer structures. We include the boundary conditions for explaining the ferromagnetic resonance spectra in the multilayer FM/AFM/FM films. The content of this chapter provides us the theoretical base for analyzing the experimental data we got from FMR and pump-probe MOKE in chapter 4 and chapter 5, respectively.

The experimental techniques we employed in our research were introduced in chapter 3. The descriptions include the preparation of samples, the experimental setups of FMR and the characterizations of our laser systems.

In chapter 4, we analyze the data from our FMR measurements using the model we developed in chapter 2. We discuss the uniform and standing wave modes in the spectrum, present the experimental fitting of angular dependence of resonance fields and extract the magnetic parameters from the fitting. Finally, we point out that the addition of surface dynamic pinning is essential for understanding our experimental results.

In chapter 5, we present data from our time-resolved pump-probe MOKE measurements. We reveal three modes from the MOKE oscillation graph by Fourier transform. The results show great consistency with our FMR data analysis. Our experiments in both time and frequency domain indicate that the surface and interface effects play an essential role in magnetic dynamics of ferromagnetic multilayer thin films.

At last, we discuss magnetic relaxation process involved in our measurements. We investigate both intrinsic and extrinsic damping contribution based on our data. We confirm two magnon scattering mechanism is dominant for extrinsic damping and surface and interface effects are crucial for the magnetic relaxation of our samples.

We conclude the dissertation with summary and outlook as chapter 7.

Chapter 2

Theory of Spin Wave Dynamics in multilayer magnetic structures

2.1 Collective Spin Wave Excitation in Multilayer Thin Films

Spin waves are the dynamic eigen-excitations of a magnetic system. The concept of spin waves, as the lowest lying magnetic states above the ground state of a magnetic medium, was introduced by Bloch [35]. He considered some of the spins as deviating slightly from their equilibrium orientation, with these disturbances propagating as a wave through the medium. The dynamic behavior of a spin is determined by the equation of motion, which can be derived from the quantum theory. The time evolution of a spin observable S is determined by its commutator with the Hamilton operator H:

$$i\hbar \frac{d}{dt} S = [S, H] \tag{5}$$

The Hamiltonian, which describes the interaction of the spin with the external magnetic field, given by its flux B, can be expressed as:

$$H = -\frac{g\mu B}{\hbar} \vec{S} \bullet \vec{B} \tag{6}$$

where μ_B is the Bohr magneton ($\mu_B < 0$) and g is the gyromagnetic factor for a free electron. The z-component of the commutator in Eq. (5) can be derived:

$$\begin{aligned}
[S_Z, H] &= -\frac{g\mu_B}{\hbar}[S_z, S_xB_x + S_yB_y + S_zB_z] \\
&= -\frac{g\mu_B}{\hbar}([S_z, S_x]B_x + [S_z, S_y]B_y) \\
&= ig\mu_B(B_yS_x + B_xS_y) \\
&= ig\mu_B(S \times B)_x
\end{aligned} \tag{7}$$

With the help of the commutation rules for spin operators:

$$[S_i, S_j] = i\hbar\varepsilon_{ijk}S_k \tag{8}$$

Corresponding expressions can be derived for the other two components of the spin, which lead to the spin equation of motion:

$$\frac{d}{dt}\langle S\rangle = \frac{g\mu B}{\hbar}(\vec{S}\times\vec{B}) \tag{9}$$

The derived equation of motion for one spin can be further generalized for the case of homogeneous magnetization within the macrospin model, considering the relation between M and $\langle S\rangle$:

$$M = \frac{g\mu B}{\hbar}\langle S\rangle \tag{10}$$

Therewith, the analogous equation of motion of magnetization in an external field H is observed as in case of one spin:

$$\frac{d}{dt}\vec{M} = -\gamma\mu_0\vec{M}\times\vec{H} = \gamma_0\vec{M}\times\vec{H} \tag{11}$$

where the gyromagnetic ratio $\gamma = g\mu B/\hbar$ is introduced and $\gamma_0 > 0$. This is well-known landau-Lifshitz equation.

The Landau-Lifshitz equation implies that the magnetization, once taken out of the equilibrium position, precesses around the external field H infinitely long. In reality, though, the magnetization eventually aligns with the external field. This experimentally observable fact demands the introduction of a dissipation term into the Landau-Lifshitz equation. To estimate the damping term, Gilbert first applied a thermodynamical approach in the following form:

$$\frac{\alpha}{M_S}\vec{M} \times \frac{d\vec{M}}{dt} \tag{12}$$

where α denotes the dimensionless Gilbert damping parameter. It determines how fast the energy of the magnetization precession is dissipated from the system. With this, the equation of motion for the magnetization is given by the Landau-Lifshitz-Gilbert (LLG) equation:

$$\frac{d\vec{M}}{dt} = -\gamma\vec{M} \times H + \frac{\alpha}{M_S}\vec{M} \times \frac{d\vec{M}}{dt} \tag{13}$$

The Gilbert damping parameter for transition metals is much smaller than 1, which allows the magnetization to make a number of precessions before it is aligned with the external field. The nature of the damping and different contributions to the energy dissipation processes are explained in detail in Chapter 6. Based on the theoretical discussion about magnetic dynamics in magnetic material, we can develop a model suitable for our trilayer FM/AFM/FM thin films [36]. In the limit of small amplitude motion, algebraic expressions for the frequencies of the various resonant modes of multilayered elements can be obtained. By neglecting the damping term we obtained the Landau-Lifshitz equation for multilayer ferromagnetic thin films:

$$\frac{\partial M_i}{\partial t} = -|\gamma_i|\left[\vec{M}_i \times \vec{H}_{eff}\right] \tag{14}$$

where the index $i = 1, 2$ denotes the magnetic layer under consideration. The total effective magnetic field acting upon layer I may be written as

$$\vec{H}_{effi} = -\frac{1}{M_i}\nabla_{ui}\vec{E}_{effi} \tag{15}$$

where E_{effi} is the effective volume energy density of layer I and the gradient is taken with respect to the components of the unit vector, $u_i = \vec{M}_i / M_i$.

The samples we investigated are FM/AFM/FM trilayer films grown on a seed layer. The sample orientation with respect to the external magnetic field and the polar coordinate system used in the subsequent discussion are plotted in Fig. 2.1. The dc magnetic field H was applied in the horizontal plane and the microwave magnetic field was along vertical direction. The sample was placed in a quartz tube inserted in the microwave cavity and rotated with respect to H in an orientation between the normal to the layer plane ($\theta = 90^o$) and the in-plane orientation ($\theta = 0^o$).

In order to determine the magnetic parameters, we can start from expression of magnetic free energy density per unit area of the film E:

$$\begin{aligned}E = \sum_{i=1,2} d_i\{&-M_iH[\cos\theta_i\cos\theta_H + \sin\theta_i\sin\theta_H\cos(\varphi_i-\varphi_H)]\\&-2\pi M_i^2\sin^2\theta_i - K_U\cos^2\theta_i - M_iH_{ei}\sin\theta_i\cos(\varphi_i-\varphi_{ei})\\&-K_A\sin^2\theta_i\cos^2(\varphi_i-\varphi_{2i})\}\\&+A_{12}[\cos\theta_1\cos\theta_2+\sin\theta_1\sin\theta_2\cos(\varphi_1-\varphi_2)]\end{aligned} \tag{16}$$

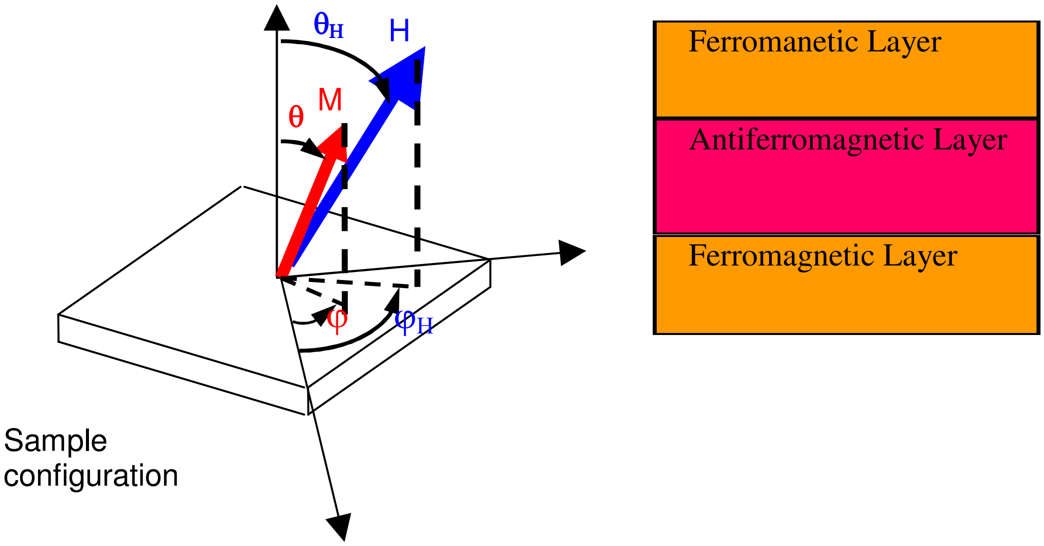

Fig. 2.1 Geometry of sample setup and structure of FM/AFM/FM samples

where, d_i, K_U, K_A, and H_{ei} are the thickness, out of plane uniaxial anisotropy constant, effective in plane anisotropy constant and exchange bias field of each ferromagnetic layer. In layer i the unit vectors u_i, k_A, k_U, and h_{ei} lie parallel to the magnetization, the uniaxial anisotropy axis, the mutually perpendicular in-plane four-fold hard axes, and the exchange bias field, respectively. The constant A_{12} determines the strength of the interlayer coupling. Here φ_i and φ_{2i} are the angles that M_i *and* $\boldsymbol{k}_A$ describe with **H**.

To derive the expression for frequency dependence on the external magnetic field by both amplitude and orientations relative to the sample magnetization, we first derive the Landau-Lifshitz equation in the spherical coordinates [5] schematically presented in Fig. 2.2,

$$\frac{d}{dt} M = -\gamma\mu_0 M \times H_{eff} \quad . \qquad (17)$$

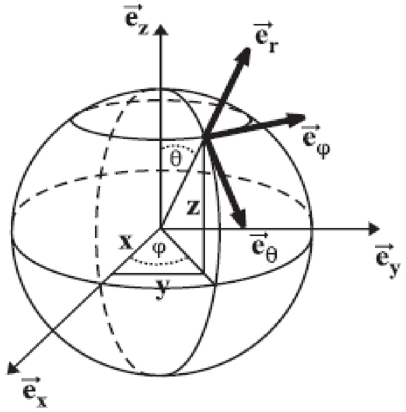

Fig. 2.2: Spherical coordinate system

The infinitesimal small change of the magnetization vector is then expressed by:

$$dM = M_S dr e_r + M_S d\theta e_\theta + M_S \sin\theta d\varphi e_\varphi ,$$

where M_s denotes saturation magnetization, and θ and φ denote the polar and azimuthal angle of M in the Cartesian coordinate system. The effective magnetic field H_{eff} can be expressed in spherical coordinates using the following expression:

$$\begin{aligned} H_{eff} &= -\frac{1}{\mu_o M_S}\frac{\partial E}{\partial m} \\ &= -\frac{1}{\mu_o}\left(\frac{\partial E}{\partial r}e_r + \frac{1}{M_S}\frac{\partial E}{\partial \theta}e_\theta + \frac{1}{M_S \sin\theta}\frac{\partial E}{\partial \varphi}\right) \end{aligned} \tag{18}$$

The left and right hand side in the Landau-Lifshitz equation Eq. (17) can then be expressed as:

$$\begin{aligned} \frac{dM}{dt} &= M_S \frac{d\theta}{dt}e_\theta + M_S \sin\theta \frac{d\varphi}{dt}e_\varphi \\ M \times H_{eff} &= \frac{1}{\mu_0 \sin\theta}\frac{\partial E}{\partial \varphi}e_\theta - \frac{1}{\mu_0}\frac{\partial E}{\partial \theta}e_\varphi \end{aligned} \tag{19}$$

which leads to the Landau-Lifshitz equation in spherical coordinates:

$$\begin{aligned}\frac{d\theta}{dt} &= -\frac{\gamma}{M_s \sin\theta}\frac{\partial E}{\partial\varphi} \\ \frac{d\varphi}{dt} &= \frac{\gamma}{M_s \sin\theta}\frac{\partial E}{\partial\theta}\end{aligned} \quad . \qquad (20)$$

For the small variations around the equilibrium position, the free energy F can be converted to a Taylor series, in which the first approximation is given by:

$$E = E_0 + \frac{1}{2}(E_{\theta\theta}\theta^2 + 2E_{\theta\varphi}\theta\varphi + E_{\varphi\varphi}\varphi^2) \qquad (21)$$

The equations of motion for the azimuthal and polar angle of the magnetization then become:

$$\frac{d\theta}{dt} = -\frac{\gamma}{M_s \sin\theta}(E_{\theta\varphi}\theta + E_{\varphi\varphi}\varphi)$$

$$\frac{d\varphi}{dt} = \frac{\gamma}{M_s \sin\theta}(E_{\theta\theta}\theta + E_{\theta\varphi}\varphi) \qquad (22)$$

The θ and φ, which satisfy the previous sets of equations, are given by the small harmonic oscillations around the equilibrium values, θ_0 and φ_0:

$$\theta - \theta_0 = \theta_A \exp(-i\omega t)$$

$$\varphi - \varphi_0 = \varphi_A \exp(-i\omega t) \qquad (23)$$

where θ_A and φ_A denote the amplitude of those precessions. The previous expressions are incorporated into Eq. (22) to derive the following set of equations:

$$\left(\frac{\gamma E_{\theta\varphi}}{M_S \sin\theta} - i\omega\right)\theta + \frac{\gamma E_{\varphi\varphi}}{M_s \sin\theta}\varphi = 0$$

$$\frac{\gamma E_{\theta\theta}}{M_s \sin\theta}\theta + \left(\frac{\gamma E_{\theta\varphi}}{M_s \sin\theta} + i\omega\right)\varphi = 0 \tag{24}$$

The non-trivial solution to the homogeneous system given by the previous equations exists only when the following condition is satisfied:

$$\omega_{res}^2 = \frac{\gamma^2}{M^2 \sin^2\theta}\left(E_{\theta\theta}E_{\varphi\varphi} - E_{\theta\varphi}^2\right). \tag{25}$$

The precession frequency is given by the partial derivatives of the free magnetic energy with respect to the azimuthal and polar angle of the magnetization *M* at their equilibrium values. We can use this formula to determine the frequency dispersion relation for different magnetic precession modes.

First, we need to compute the value of $\frac{\partial}{\partial\theta}(\frac{\partial E}{\partial\theta_i})$, $\frac{\partial}{\partial\varphi}(\frac{\partial E}{\partial\varphi_i})$ and $\frac{\partial}{\partial\theta}(\frac{\partial E}{\partial\varphi_i})$.

$$\begin{aligned}\frac{\partial}{\partial\theta}\left(\frac{\partial E}{\partial\theta_i}\right) &= \sum_{i=1,2} d_i\{M_i H \sin\theta_H \sin\theta_i \cos(\varphi - \varphi_i)\\ &+ 4\pi M_i^2 \cos 2\theta_i + 2K_U \cos 2\theta_i + M_i H_{ei} \sin\theta_i \cos(\varphi_i - \varphi_{ei})\\ &+ 2K_A \cos 2\theta_i \cos^2(\varphi_i - \varphi_{2i})\} - A_{12}[-\cos\theta_1 \cos\theta_2 - \sin\theta_1 \sin\theta_2 \cos(\varphi_1 - \varphi_2)]\end{aligned} \tag{26}$$

$$\begin{aligned}\frac{\partial}{\partial\varphi}\left(\frac{\partial E}{\partial\varphi_i}\right) &= \sum_{i=1,2} d_i\{M_i H \sin\theta_H \sin\theta_i \cos(\varphi_i - \varphi_H) + M_i H_{ei} \sin\theta_i \cos(\varphi_i - \varphi_{ei})\\ &+ 2K_A \sin^2\theta_i \cos^2(\varphi_i - \varphi_{2i})\} - A_{12} \sin\theta_1 \sin\theta_2 \cos(\varphi_1 - \varphi_2)\end{aligned} \tag{27}$$

As a special case, we consider the applied field is in plane, and we know the magnetization vector will press about the external field by small amplitude, thus we can simplify the expressions:

$$\begin{gathered}\frac{\partial}{\partial\theta}\left(\frac{\partial E}{\partial\theta_i}\right)=\sum_{i=1,2} d_i\{M_i H\cos\varphi_i+4\pi M_i-2K_{2\perp}\\+M_i H_{ei}\cos(\varphi_i-\varphi_{ei})+2K_A\cos^2(\varphi_i-\varphi_{2i})\}-A_{12}\cos(\varphi_1-\varphi_2)\end{gathered}\tag{28}$$

and

$$\begin{gathered}\frac{\partial}{\partial\varphi}\left(\frac{\partial E}{\partial\varphi_i}\right)=\sum_{i=1,2} d_i\{M_i H\cos\varphi_i+M_i H_{ei}\cos(\varphi_i-\varphi_{ei})\\+2K_A\cos^2(\varphi_i-\varphi_{2i})\}-A_{12}\cos(\varphi_1-\varphi_2)\end{gathered}.\tag{29}$$

Also we got $\frac{\partial}{\partial\theta}\left(\frac{\partial E}{\partial\varphi_i}\right)=0$. We use:

$$\omega_{res}^2=\frac{\gamma^2}{M^2\sin^2\theta}(E_{\theta\theta}E_{\varphi\varphi}-E_{\theta\varphi}^2)\tag{30}$$

for small deviation from the static equilibrium.

Then we can have

$$\begin{gathered}\omega^2=\frac{1}{2}\{(F_1G_1+F_2G_2+B_1C_2+B_2C_1)\pm[(F_1G_1+F_2G_2+B_1C_2+B_2C_1)^2\\+4(G_1G_2-B_1B_2)(C_1C_2-F_2F_1)]^{1/2}\}\end{gathered}\tag{31}$$

in which

$$\begin{gathered}F_i=\gamma_i[H\cos\varphi_i+H_{ei}\cos(\varphi_i-\varphi_{ei})\\+\frac{2K_A}{M_i}\cos 2(\varphi_i-\varphi_{2i})-\frac{A_{12}}{M_i d_i}\cos(\varphi_1-\varphi_2)]\end{gathered}\tag{32}$$

$$\begin{aligned} G_i = \gamma_i[&H\cos\varphi_i + H_{ei}\cos(\varphi_i - \varphi_{ei}) \\ &+ \frac{2K_U}{M_i}\cos^2(\varphi_i - \varphi_{2i}) + 4\pi M_i - \frac{A_{12}}{M_i d_i}\cos(\varphi_1 - \varphi_2)] \end{aligned} \tag{33}$$

$$B_i = \frac{\gamma_i A_{12}}{M_i d_i}\,, \tag{34}$$

$$C_i = B_i\cos(\varphi_1 - \varphi_2)\,. \tag{35}$$

The angle φ_i is either obtained from the calculation of the static configuration or else assumed to be zero when the static field strength is sufficiently large. Equation (31) predicts that two resonant modes will occur.

In the absence of interlayer coupling, these are simply the uniform mode solutions for the individual layers, given by

$$\begin{aligned} \omega^2 = \gamma^2&[H\cos\varphi + H_e\cos(\varphi - \varphi_e) + \frac{2K_A}{M}\cos 2(\varphi - \varphi_2) \pm Dk^2] \\ &\times[H\cos\varphi + H_e\cos(\varphi - \varphi_e) - \frac{2K_U}{M_i} + \frac{2K_A}{M}\sin^2(\varphi - \varphi_2) + 4\pi M \pm Dk^2] \end{aligned}\,. \tag{36}$$

They correspond to “acoustic” and “optical” modes in which the magnetizations of the two layers precess in and out of phase respectively [37].

Equations (31) and (36) may be used to simulate the dependence of the observed mode frequencies upon the strength and orientation of the static field, allowing the values of the anisotropy, exchange bias and exchange coupling constants to be deduced.

2.2 Dynamic Surface Pinning Conditions

In last section, we discuss the theoretical model for our multilayer FM/AFM/FM thin films and derived dispersion relation for the trilayer model. As we can see from Eq. (36), magnetic excitation frequency depends on the wave vector of spin wave. The spin wave propagation in films is closely related to the boundary conditions. Studies about boundary conditions, particularly surface pinning conditions, become essential for understanding magnetic dynamics in our multilayer thin films. Therefore, recent investigators have showed great interests in the origin and nature of the surface anisotropy which gives rise to pinning of the surface spins.

In the study of spin wave excitation in a ferromagnet, Kittel assumed that the local symmetry of a spin at the surface is always lower than the symmetry of a spin in the interior. In other words, the spins are pinned at the surface. However, people realized that Kittel's boundary conditions are not sufficient to describe the surface pinning of the magnetic metallic thin films and surface energy does contribute to the spin wave energy [38]. The first observation of signals due to the surface states in the SWR spectra in permalloy was reported by Salanskii and Mikhailovskii [39]. Subsequent discoveries of surface spin wave excitations in other material have stimulated studies of surface states. In this context, various theoretical models have been proposed. In Valenta's model, a physical "individuality" is attributed to each layer; so it is called Volume Inhomogeneity (VI) model. Its extreme opposite is the Puszkarski's Surface Inhomogeneity (SI) model, which distinguishes the surface layers, and considers all the other layers as mutually equivalent [40]. The SI model has shown great success in the analysis of multilayer magnetic thin films.

At surfaces of a ferromagnetic film there exists a surface anisotropy field which allows the excitation of an exchange-dominated nonpropagating surface mode and that there will be a critical orientation where only a single uniform FMR mode is observed. According to Puszkarski's surface inhomogeneity SI model, the actual eigenmodes are selected by the boundary conditions which in turn depend on dynamical surface spin pinning condition. The spin pinning condition at each film surface can be described by an effective parameter (K_{surf}). Following the theory of surface states in FMR, the change of spin energy at each film surface and interface can be described by an effective parameter:

$$K_S(\theta, \varphi) = \frac{dM}{z}(\vec{m} \bullet \vec{K}_{surf}) \qquad (37)$$

where z is the number of nearest-neighbor spins in a crystal lattice, d is the lattice constant, and $\vec{m}$ is the unit vector of magnetization.

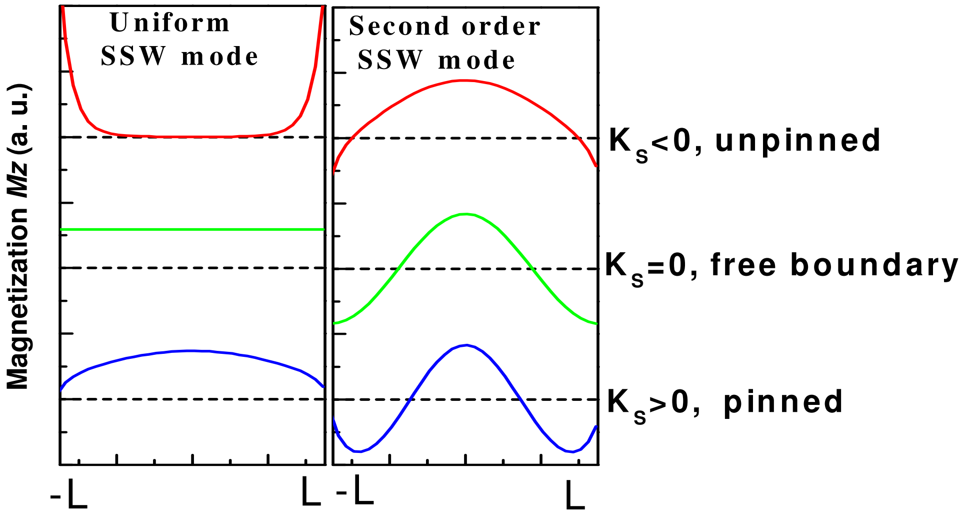

Fig. 2.3 Magnetization profile of ferromagnetic layer of thin film. Note the layer has symmetric surface on both sides.

The value of K_s gives us a dynamic measurement of the spin pinning at the surface. The effective surface anisotropy field $\vec{K}_{surf}$ is a constant vector, $\vec{m}$ is the unit vector of the magnetization M which is changing with the rotation of the sample. When the direction of $\vec{K}_{surf}$ turns to become perpendicular to $\vec{m}$, $\vec{m} \bullet \vec{K}_{surf} = 0$, thus $K_S = 0$, this orientation corresponds to the free boundary condition. When we rotate the sample to make $\vec{m}$ to align with surface anisotropy vector $\vec{K}_{surf}$, $K_S > 0$, surface anisotropy field reaches its maximum and surface spins are strongly pinned. Similarly, when $\vec{m}$ is in opposite direction with $\vec{K}_{surf}$, $K_S < 0$, surface spins are unpinned and nonpropagating surface modes could be observed.

In addition, the uniform spin wave mode can also be shifted if we consider the contribution of the surface anisotropy field in the free energy density. The energy of all the spins present per unit area of the surface can be written as [41]:

$$E_S = -\frac{Sg\mu_B}{d^2}(\vec{m} \bullet \vec{K}_{surf}) \tag{38}$$

where S is the atom spin. Since $\vec{m}$ rotates with external magnetic field, we have E_S changing with the orientation of H. In order to understand the magnetic excitation dynamics in multilayer thin films, we should consider the surface anisotropy energy and the dynamical surface spin excitations, this is extremely important for designing magnetoelectronic devices based on nanoscale structures.

The magnetic anisotropy fields must differ by some amount in the bulk and surface regions. The fact that the magnetic anisotropy field is different in the surface region (there exists a surface anisotropy field) is the essential mechanism determining surface spin pinning and thus the characterization of the FM/AFM/FM multilayer thin films.

Chapter 3

Experimental Techniques

3.1 Sample preparation

FM/AFM/FM trilayers of *CoFe/PtMn/CoFe* seeded with 30 Å of *Ru* or *NiFeCr* layer (referred to as $Co_{90}Fe_{10}[Ru]$ in the context) were deposited on oxidized silicon coupons by dc magnetron sputtering with base pressures in the order of 10^{-9} Torr [42]. To compare the seed layer effects, multilayer of $Co_{84}Fe_{16}/Pt_{50}Mn_{50}/Co_{84}Fe_{16}$ with a 30 Å *NiFeCr* seed and cap layer (referred to as $Co_{84}Fe_{16}[NiFeCr]$)) were also deposited and prepared in Prof. N. X. Sun's lab in Northeastern University [43].

The thicknesses of ferromagnetic *CoFe* layer were varied from 10 Å to 500 Å, while that of the AFM *PtMn* layer has been fixed at 120 Å. Multilayers with eight periods of the $Co_{90}Fe_{10}[Ru]$ and $Co_{84}Fe_{16}[Ru]$ trilayer structures alternated with Al_2O_3, $Al_2O_3/Co_{90}Fe_{10}[Ru]$, and $Al_2O_3/Co_{84}Fe_{16}$ were deposited with a fixed *CoFe* layer thickness of 200 Å, and with 100 Å Al_2O_3 dielectric layers to suppress eddy current loss. The sample structure is illustrated below:

Sample	CoFe	CoFe	Period
NS022	10	10	1
NS023	15	15	1
NS024	20	20	1
NS025	25	25	1
NS026	50	50	1
NS027	100	100	1
NS028	200	200	1
NS029	300	300	1
NS02A	400	400	1
NS02B	500	500	1
NS02C	200	200	8

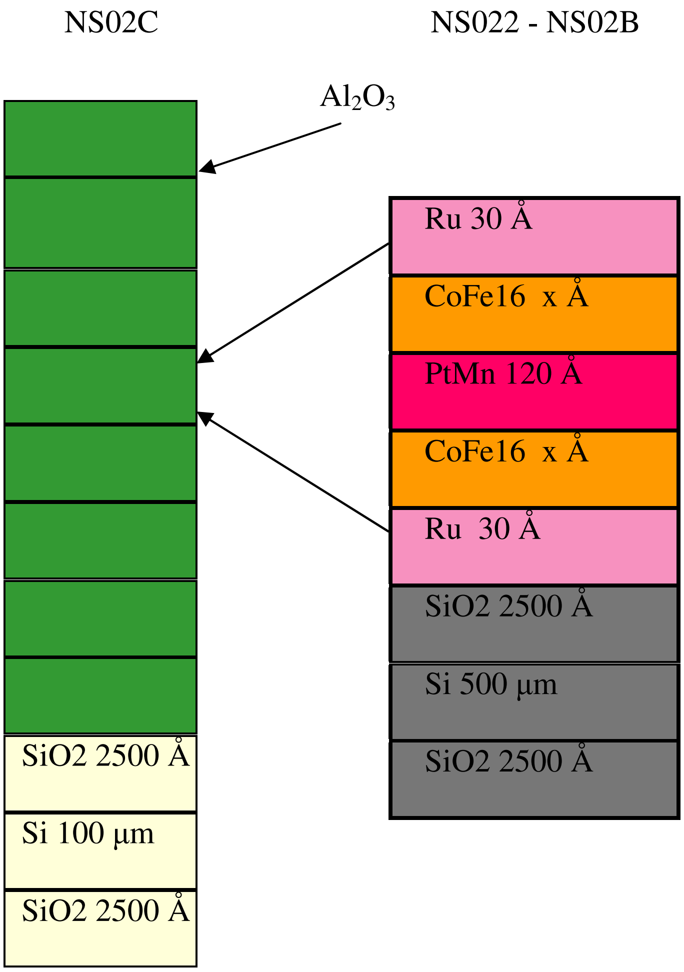

Fig. 3.1 Sample structure and configuration.

Magnetic-field annealing was carried out for these films to induce the unidirectional anisotropy field by exchange coupling before characterizing these films. The hysteresis loops along the easy axis show clear hysteresis loop shift due to exchange coupling from the AFM layer, while the hard axis hysteresis loops are typically slim with no hysteresis shift [44]. Effective anisotropy fields of these magnetic films were measured by extrapolating the hard axis minor hysteresis loops (50% saturated), a standard method for extracting anisotropy fields for magnetic materials. Magnetic field such as coercive fields, exchange coupling fields, etc., were all measured with a VSM with an error of < 1 Oe.

The *Ru*-seeded *CoFe/PtMn/CoFe* sandwich structures show excellent magnetic softness with a low hard axis coercivity of 2 – 4 Oe, an easy axis Mr/Ms of > 98%, and significantly enhanced in-plane anisotropy of 57 – 123 Oe [45,46].

3.2 FMR setup

Our FMR measurements were carried out at X-band (~9.74 GHz) using a Bruker EMX electron paramagnetic resonance (EPR) spectrometer.

Electron Paramagnetic Resonance Spectroscopy is a technique that is used to obtain specific physical and chemical characteristics from a sample. It is usually used as an supplementary method to other forms of spectroscopy. It works by detecting unpaired electrons in samples in a magnetic field. Ferromagnetic resonance (FMR) is a special case of EPR, in which the individual electron spins are strongly interacting, as in the case of ferromagnetic materials.

The microwave radiation travels down a waveguide (a type of rf pipe) to the sample, which is held in place in a microwave ‘cavity’ held between the poles of two magnets. Spectra are obtained by measuring the absorption of the microwave radiation while scanning the magnetic-field strength. EPR spectra are usually displayed in derivative form to improve the signal-to-noise ratio. FMR is a sensitive technique capable to measure thin films. Resonance line can be determined with 0.1 mT resolution. Compared to classical magnetometers (Vibrating Sample Magnetometer or SQUID

Magnetometer) the substrate signal resonates at fields very different from the sample's ones and magnetization (not magnetic moment) is directly measured (no need to know precisely the volume of the sample). Another information from FMR is about the homogeneity of the sample (related to the width of the resonance line) [47].

The angular dependence in the FMR experiments provides information about the anisotropic constants – parameters that are crucial for the design of thin film devices. In ferromagnetic material atoms effectively act as atomic bar magnets which interact co-operatively so that large groups of atoms within a structure have a common orientation of their magnetism. In a quantum mechanical description, the alignment of magnet moments is ascribed to the exchange interaction, which energetically favors magnetic order.

A ferromagnetic sample is located in a strong magnetic field. The effect of the strong magnetic field is to align the atomic magnetic moments in a single orientation, and to alter the energy levels of excited states of the atoms. Microwave radiation at a predetermined frequency is directed at the sample. The strength of the magnetic field is increased gradually, thereby altering the degree of alignment of the atoms and modifying the energy levels of the excited states of the atoms. When an energy level of an excited state is equal to the energy of the incident microwave photons, the microwave radiation will be resonantly absorbed by the ferromagnetic material [48].

The Bruker EMX 200U EPR is a Continuous Wave (CW) sweep EPR, equipped with an ER4102ST universal X-band resonator, rectangular TE102 cavity, operating at a nominal frequency of 9.74 GHz [49]. The EMX Signal Channel can be operated at any modulation frequency between 6 kHz and 100 kHz, and has unsurpassed phase resolution and stability. It incorporates automatic digital tuning of any cavity to any modulation frequency, without using the classical "tuning-box" required with each cavity. A high stability, digitally controlled Hall field controller allows you to sweep the magnetic field to over 8,000 Gauss (0.8 Tesla) and set field values with a resolution of under 1 mG (0.1 μT). The field is produced by a water-cooled magnet with a pole diameter of 10 inches, and air gap of 64 mm, using a 2.7 kW power supply.

FMR linewidth of these films was measured by using the field sweep FMR/electron paramagnetic resonance (FMR/EPR) facility with both dc magnetic field and microwave excitation field in the plane of the thin-film samples. Due to weak FMR absorption signal in the FMR spectra, only samples with t_F at or above 50 Å were measured.

Fig. 3.2 Bruker X-band EPR spectrometer

The sample orientation in the sweeping field is plotted in Fig. 2.1 (which clearly indicates out-of-plane configuration). The orientation of the dc magnetic field H is described by θ_H and φ_H, the resulting equilibrium orientation of the magnetization M is given by θ and φ. The samples were placed in a quartz tube inserted in the microwave cavity and rotated with respect to H in an orientation either in the layer plane (change φ) or along the out-of-plane configuration (between the in-plane orientation $\theta_H = 90^o$ and the normal to the layer plane ($\theta_H = 0^o$).

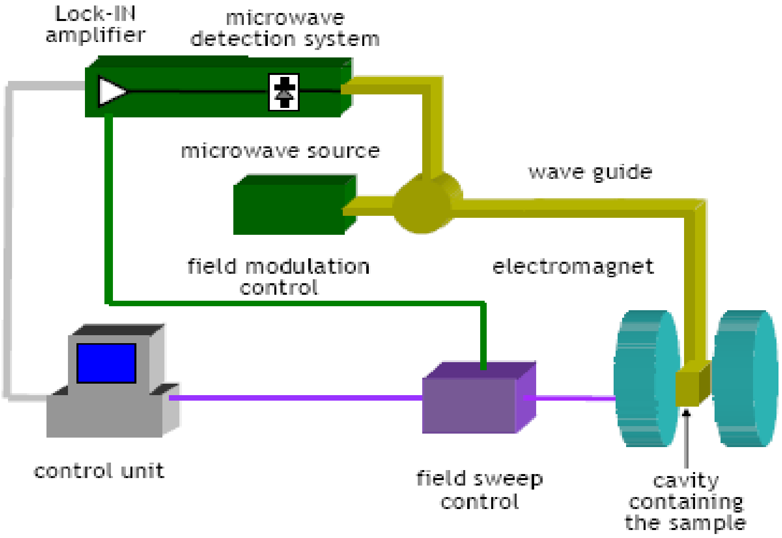

Fig. 3.3 Scheme of our FMR assembly

3.3 Ultrafast Magneto-Optical Spectroscopy

3.3.1 Laser System

The development of femtosecond laser systems has opened the door for investigating ultrafast dynamical processes, which range from nuclear motion in molecules to relaxation mechanisms of charge carriers in solids. A characteristic of the approach is that the system investigated is no longer in thermodynamic equilibrium. It is rather in an excited state whose decay into electronic-, spin-, and lattice- degree of freedom is being probed.

The femtosecond laser system in our laboratory comprises the diode-pumped Frequency-Doubled cw-*Nd*:vanadate Laser (*Millennia Pro 5i, Spectra-Physics*) and a broadband tunable Ti:sapphire Oscillator (*Tsunami, Spectra-Physics*) [41, 42]. The Ti:Sapphire oscillator, based on passive Kerr mode locking, produces 70fs pulses at λc =780nm at a repetition rate of 80MHz. The energy per pulse is approximately 1nJ. We use an optical Spectrum Analyzer (*Newport*) to optimize laser wavelength and linewidth. Optical cryostats (*VPF-100 and ST-300, Janis*) were used for our low-temperature studies. An electromagnet (*GMW 5403)* was employed for the magnetic field dependent measurements.

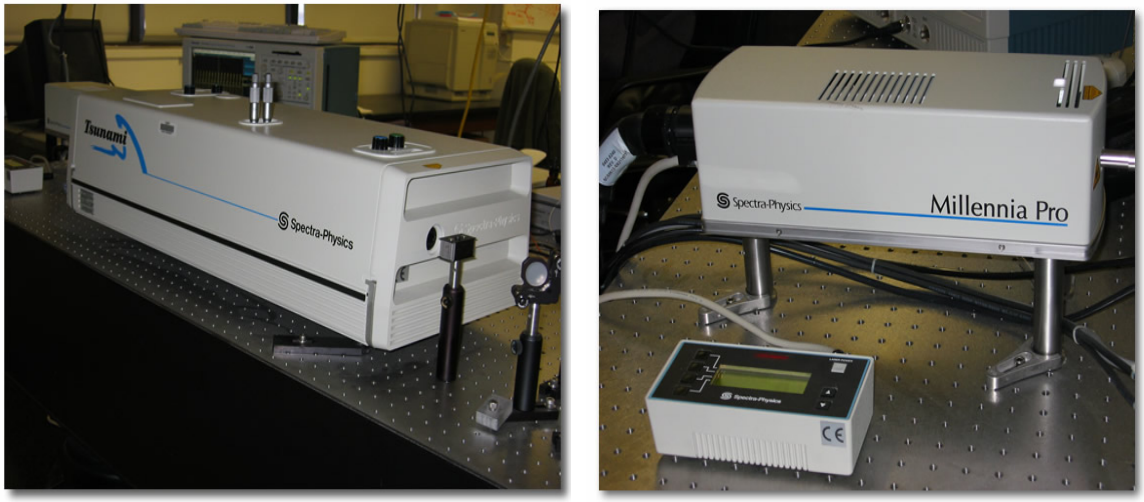

Fig. 3.4 Broadband Tunable Ti:sapphire Oscillator and Diode-Pumped Frequency-Doubled cw-Nd: vanadate Laser

3.3.2 Beam Characterization

3.3.2.1 *Laser wavelength and linewidth (optical spectrometer)*

Optical spectrum analyzers (OSA) display the emission spectrum of the source rather than a numerical value of the wavelength of the laser line as in the case of a wavemeter. Typically, wavemeters have accuracies ~1 pm while OSA has a resolution of 0.1 nm and a sensitivity of ~100 pW over the range 0.6 – 1.6 µm. OSA displays the actual laser emission spectrum. OSAs were calibrated against either wavemeters or reference laser lines [51].

We used the optical spectrum analyzer to optimize the wavelength and linewidth of our lasers. OSA can divide a light wave signal into its constituent wavelengths. This means that it is possible to see the spectral profile of the signal over a certain wavelength range. The profile is graphically displayed, with wavelength on the horizontal axis and power on the vertical axis. The spectrum analyzer displays a power spectrum over a given frequency range in real time, changing the display as the properties of the signal change. In this way, the many signals combined on a single fiber in a dense wavelength division multiplexing (DWDM) system can be taken apart to perform per-channel analysis of the optical signal and its spectral interaction with the other wavelengths. . A fiber optic cable is used to couple the output from the test device into the spectrometer. The instrument allows characterization of the wavelength stability with time at high resolution spectrometers up to 0.1nm resolution.

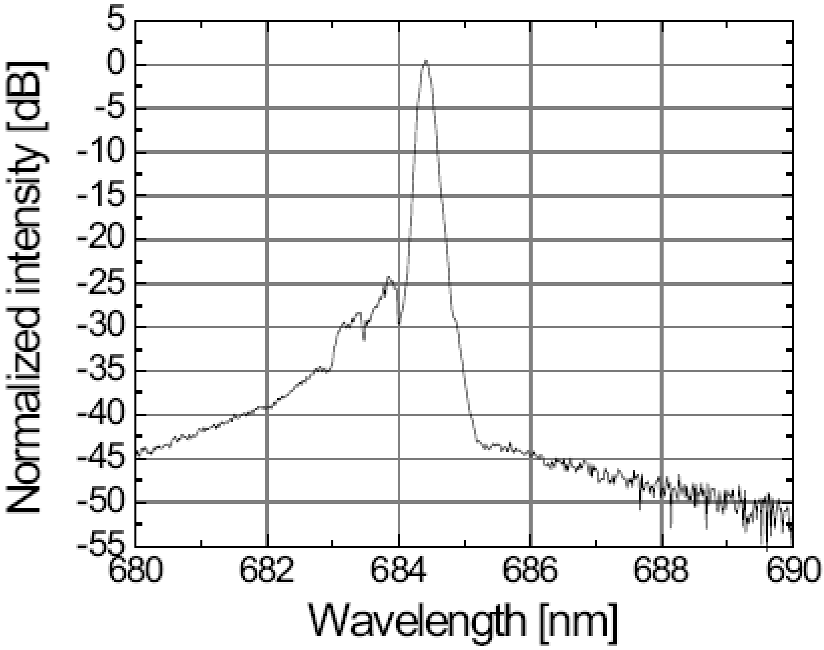

Fig. 3.5 Wavelength and linewidth stabilization and optimization by optical spectrum analyzer

3.3.2.2 *Laser Pulse Compression (Prism Pair)*

Femtosecond lasers are the most popular form of tunable laser in use today. Their inherent peak power allows for efficient nonlinear frequency conversion that results in the broadest spectral coverage of any type of laser. Furthermore, the high peak intensities of ultrafast pulses aid in the study of various samples. However, ultrafast pulses present a set of unique challenges that often limit their ultimate effectiveness. Typically, a phenomenon called group-velocity dispersion (GVD), which broadens the ultrafast pulses as they pass through optical elements in the microscope, significantly reduces the imaging depth [52].

Dispersion is the phenomenon in which the phase velocity of a wave depends on its frequency. Group-velocity dispersion can be described as a delay of shorter wavelengths with respect to longer wavelengths within the ultrafast pulse as it passes through an optical medium.

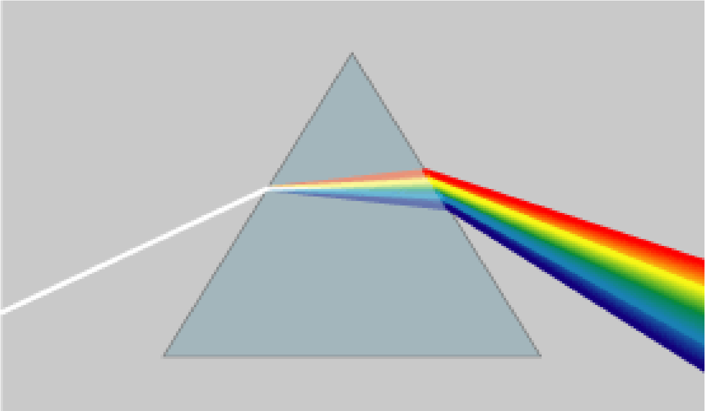

Fig. 3.6 Light dispersion by a prism

Dispersion compensation essentially means canceling the chromatic dispersion, avoiding excessive temporal broadening of ultra-short pulses and/or the distortion of signals. We used prism pair to compensate the negative dispersion introduced by various optic elements in our experiment. Although the additional glass of the prisms introduces additional positive dispersion, the spacing between them introduces negative dispersion, delaying longer-wavelength components. Altering the distance between the prisms allows for the adjustment of the maximum possible negative dispersion provided by the prism pair; thus, sufficient compensation is always possible if enough space is available to separate the prisms.

Pairs of (typically Brewster-angled) prisms can be used for introducing anomalous chromatic dispersion without introducing significant power losses. A first prism refracts different wavelength components to slightly different angles. A second prism then refracts all components again to let them propagate in parallel directions after that prism (see Figure 3.7), but with a wavelength-dependent position (which is sometimes called a *spatial chirp*). With a second prism pair, or simply by reflecting the beams back through the original prism pair, all wavelength components can later be spatially recombined

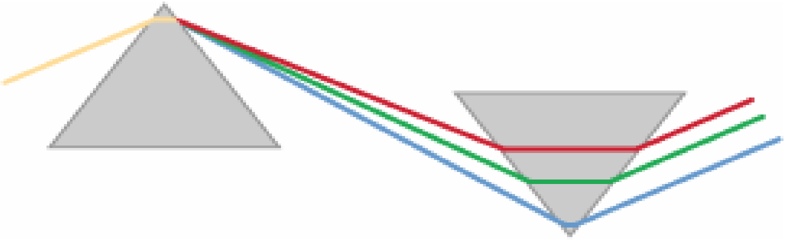

Fig. 3.7: A prism pair spatially disperses different wavelength components and thus also introduces wavelength-dependent phase changes.

The wavelength-dependent optical path lengths of dispersive delay line usually lead to positive dispersion [53], which may be partly offset by material dispersion in the prisms. The overall dispersion can be adjusted by varying the separation between the two prisms. By using the prism pairs; we achieved a very short pulse width of 300 fs , which is down from 800fs without prism pairs setup. Below is schematic setup for our prism pairs:

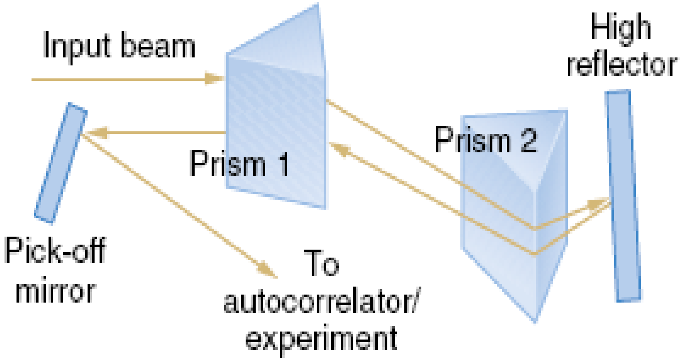

Figure 3.8: Compensate dispersion using prism pairs

3.3.2.3 *Autocorrelation*

We optimize the pulse width of our laser beams by an autocorrelation setup. The intensity autocorrelation was the first technique used to measure the intensity vs. time of an ultrashort laser pulse. Early on (the 1960's), it was realized that no shorter event existed with which to measure an ultrashort pulse. And the autocorrelation is what results when a pulse is used to measure itself. It involves splitting the pulse into two, variably delaying one with respect to the other, and spatially overlapping the two pulses in some instantaneously responding nonlinear-optical medium, such as a second-harmonic-generation (SHG) crystal (in our experiments, A BBO (beta barium borate) crystal is used) [54]. Optical autocorrelators are used for various purposes, in particular for the measurements of the duration of ultrashort pulses with picosecond or femtosecond durations, where an electronic apparatus (based on, e.g., a photodiode) would be too slow.

A SHG crystal will produce "signal light" at twice the frequency of input light with a field envelope that is given by:

$$E_{sig}^{SHG}(t,\tau) \propto E(t)\; E(t-\tau) \qquad (39)$$

where τ is the delay. This field has an intensity which is proportional to the product of the intensities of the two input pulses:

$$I_{sig}^{SHG}(t,\tau) \propto I(t)\; I(t-\tau) \;. \qquad (40)$$

Detectors are too slow to resolve this beam in time, so they'll measure:

$$A^{(2)}(\tau) = \int_{-\infty}^{\infty} I(t)\, I(t-\tau)\, dt \qquad (41)$$

This is the intensity autocorrelation. The superscript (2) implies that it's a second-order autocorrelation; third-order autocorrelations are possible, too. Below is shown the setup for intensity autocorrelation using BBO crystal:

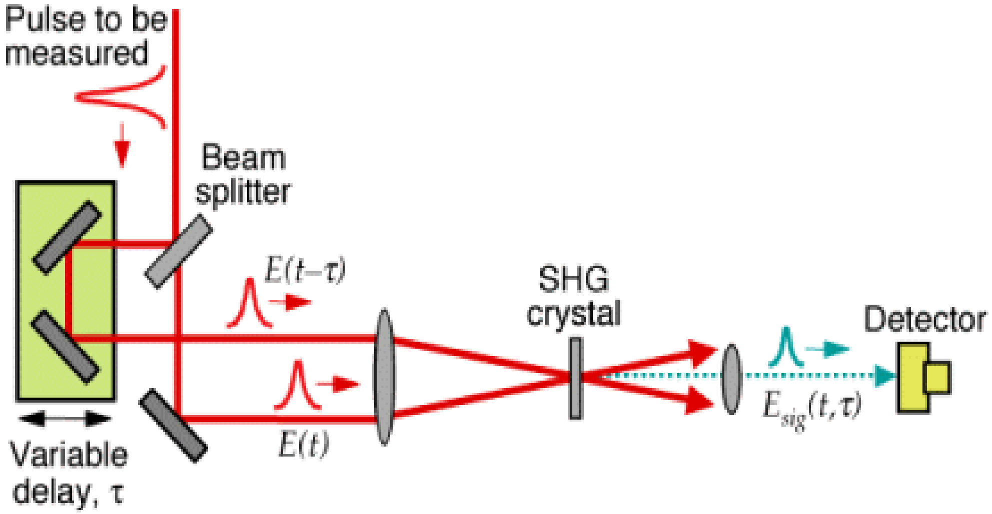

Fig.3.9: Experimental layout for intensity autocorrelation using second-harmonic generation.

In Fig. 3.9, a pulse is split into two, one is variably delayed with respect to the other, and the two pulses are overlapped in an SHG crystal. The SHG pulse energy is measured vs. delay, yielding the autocorrelation trace. Other nonlinear-optical effects, such as two-photon fluorescence and two-photon absorption can also yield the autocorrelation, using similar beam geometries.

3.3.3 Pump-probe MOKE

We employed the time-resolved MOKE to investigate spin and magnetization dynamics as shown in Fig. 3.10. The pump beam create a non-equilibrium spin population, and the subsequent magnetization precession and spin-relaxation will be probed by transient Kerr-rotation (or Faraday rotation) of a linearly-polarized probe beam as a function of time delay between the two pulses. To optimize the optical signal to noise ratio, we set the spot sizes of the pump and probe beams to 10 and 20 μm, respectively, and adopt a double lock-in technique [55,56]. In this configuration, a photo-elastic modulator varies the polarization of the probe at 50 kHz. The signal will be filtered by a lock-in amplifier operating at 50 or 100 kHz, to obtain the ellipticity and the rotation. The output signal will be then processed by a second lock-in amplifier referenced to a 150-Hz chopper on the pump beam. The measurements will be taken in the Voigt or Faraday geometry as a function of the applied magnetic field. The pump beam perturbs the spin states either by 1) "thermal" pumping, in which a hot electron gas is excited, which heats the lattice and causes a loss of the magnetization [57]; 2) "electrical" or "magnetic" pumping, in which a photoconductive switch is used to create electronic spin injection or modify the magnetization by means of an ultrafast magnetic pulse along a transmission line [58]; or 3) "magneto-optical" or "circularly polarized" pumping, in which spin selective optical excitations cause a change in the equilibrium spin density. In the experiments we conducted recently, we mainly focus our time-resolved measurements in the visible and near infrared range (400 nm ~ 800 nm) [59].

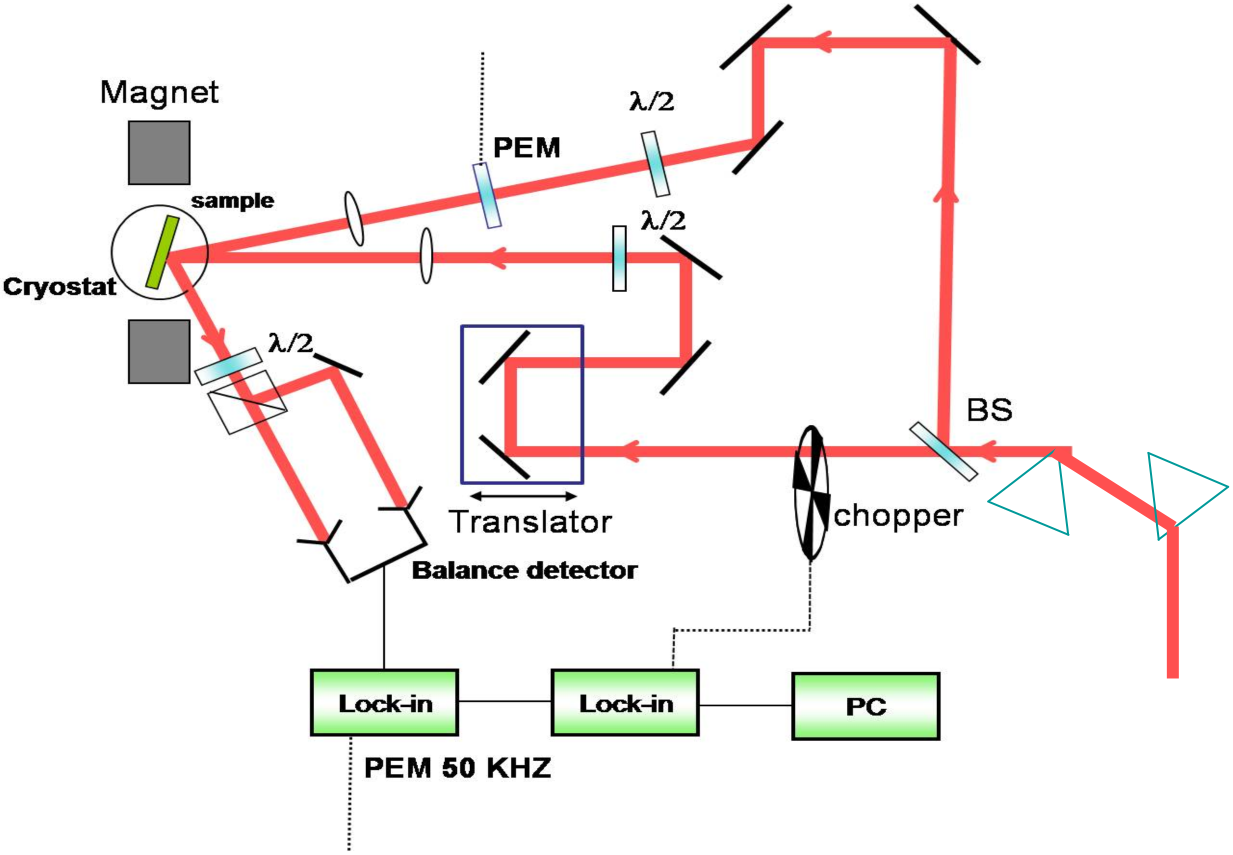

Fig. 3.10: Schematic of the time-resolved MOKE setup. BS: beam splitter

The damping constant is estimated by fitting the time-domain experimental data into Landau-Lifshitz or Gilbert equation. The Gilbert damping constant for permalloy is determined to be 0.008 by this method [60]. The optical measurements in this technique are performed with pico-second pulses delivered by a synchronously pumped laser and the polar [61] or transverse [62] Kerr rotation monitored by a polarizing beam splitter and balance detection scheme, which measures the linear MOKE signal.

Chapter 4

Spin Wave Dynamics in Frequency Domain

We investigated the magnetic anisotropic properties and the spin wave relaxation in single and eight periods of trilayer films of *CoFe/PtMn/CoFe* grown on the seed layer *Ru* or *NiFeCr* with *CoFe* compositions being *Co*-16 at % Fe. The measurements were taken in samples with the ferromagnetic layers of *CoFe* varying from 10 Å to 500 Å by the Bruker EPR system using ferromagnetic resonance (FMR) technique. The magnetic anisotropic parameters were investigated by rotating the field aligned axis with respect to the spectral field in the configurations of both in-plane and out-of-plane.

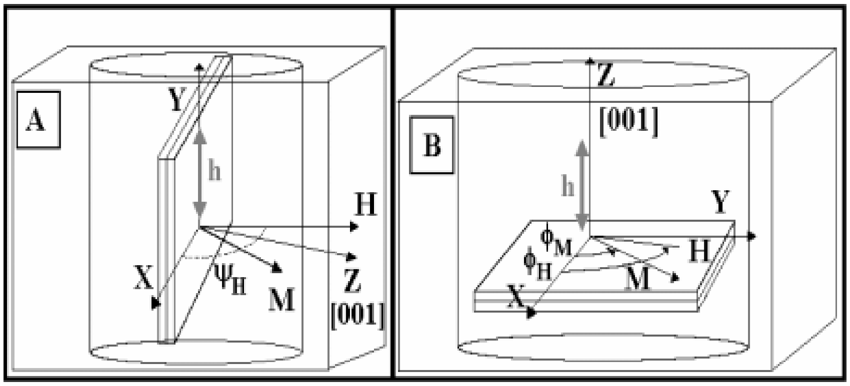

Fig. 4.1: Out-of-plane (A) and in-plane (B) configuration for samples in external magnetic field

4.1 **Uniform and standing spin wave modes**

Below are the graphs of differential resonance fields for various angles. The corresponding samples are NS028 with ferromagnetic layer thickness of 200 Å and NS02A with ferromagnetic layer thickness of 400 Å.

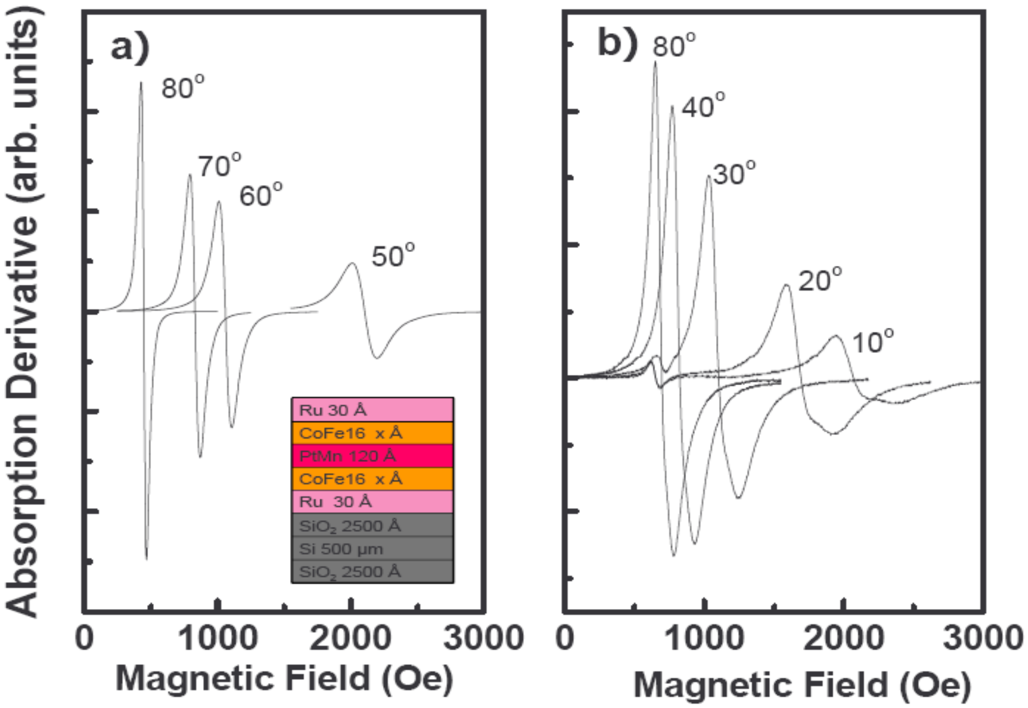

Fig. 4.2: Spin-wave resonance spectra for various magnetic field orientations in the sample (a) with 200 Å layers of CoFe and (b) with 400 Å layers of CoFe in the out-of-plane configuration. The inset shows the sample configuration.

Figure 4.2(a) shows ferromagnetic resonance spectra for various magnetic field orientations in a sample with 200 Å layers of *CoFe* in the out-of-plane configuration. As the direction of the magnetic field approaches to the film normal, the resonance line shifts a few kOe to higher fields. The line shift is induced by the demagnetizing field. For a thin film sample, a macroscopic magnetization could produce a field of 4πM, which usually points along the perpendicular direction of the sample plane. When we rotated our sample with respect to the applied magnetic field, the equilibrium angle of the magnetization vector depends strongly on the external field value. Therefore, we expect to see a shift of FMR line and an increase of their linewidth at an intermediate angle [63]. This effect is more obvious in the FMR spectra of the sample with 400 Å layers of *CoFe*, which could be explained by the excitation of an exchange-dominated surface spin wave excitation. As shown in Fig. 4.2(b), in addition to the observation of the FMR line shift and broadening, we notice a significant change of the line shape. The lines show strong asymmetric behaviors with respect to the base line. The asymmetric behavior of the absorption curve could come from the overlap of the surface and uniform spin wave modes. As discussed by Vittoria et al [64],

The surface impedance shows a strong dependence on the thickness of the FM layers as well as the interlayer exchange coupling between layers [65, 66], therefore, on the angle between the external field and film normal.

We use the FMR resonance lines and their linewidths to determine the dynamical magnetic properties of the trilayers of *CoFe/PtMn/CoFe.* We employ the Landau-Lifshitz-Gilbert equation of motion to describe our results:

$$\partial M / \partial t = \gamma M \times [H - \nabla_M E_A + DM^{-1} \nabla^2 M] - \frac{\alpha}{\gamma M_S} M \times \frac{dM}{dt}, \qquad (42)$$

where

$$E_A = \sum_{i=1,2} (-2\pi M_i^2 t_F \sin^2\theta_i - K_U t_F \cos^2\theta_i$$
$$- K_A t_F \sin^2\theta_i \sin^2\phi_i - M_i H_{ei} \cos\theta_i \cos\phi_i) + JM_1.M_2 \qquad (43)$$

is the demagnetization field, the magnetic anisotropy, and interlayer exchange contributions for the ferromagnetic layers to the free-energy [67]. t_F is the thickness of the ferromagnetic layer, K_U and K_A are the out-of-plane uniaxial and the effective in-plane anisotropy constants, H_{ei} is the exchange bias field between the *CoFe* layer and *PtMn* layer, J is the interlayer exchange constant, H is the external field, M_s is the saturation magnetization, and is the gyromagnetic factor. γ is the dimensionless damping coefficient (Gilbert damping constant) and D is the spin stiffness describing the exchange interactions in the films. The excitation of the spin waves is due to the absorption of microwave.

Indeed, when the applied field is rotating along the out-of-plane direction (keep $\varphi= 0^o$), the resonance frequency follows

$$\omega^2 = \gamma^2[H_R \cos(\theta_H - \theta) - (4\pi M - \frac{2K_U}{M})\cos 2\theta \pm Dk^2]$$
$$\times [H_R \cos(\theta_H - \theta) + (-4\pi M + \frac{2K_U}{M})\cos^2\theta - \frac{2K_A}{M} \pm Dk^2] \qquad (44)$$

Here K_U and K_A are out-of-plane uniaxial and effective in-plane anisotropy constants, and H is the external field strength. We neglect the exchange bias field between the *CoFe* layer and the *PtMn* layer since $H_{ei} \sim 0$ when the thickness of *CoFe* layer is ~ 400 Å. This is further confirmed by our magnetization measurement.

In Equation 44, H_R is the resonance field, $4\pi M - \frac{2K_U}{M}$, the saturation magnetization reduced by the uniaxial perpendicular anisotropy field gives an effective magnetization and k is the effective wave vector of a spin wave mode. For all studied thicknesses, we neglect the exchange bias field between the *CoFe* layer and the *PtMn* layer according to the VSM hysteresis results on the *CoFe/PtMn/CoFe* samples [68]. The interlayer exchange interaction between the *CoFe* layers is small due to their large separation.

As the applied field and the magnetization align along the in-plane direction, we have a solution for the in-phase spin wave precession including both the bulk and the surface contributions. We included the exchange interaction term in the Hamiltonian of the system [69]. The eigenfrequencies of the acoustic modes are:

$$\begin{aligned} \omega^2 &= \gamma^2 [H_R - \frac{2K_A}{M} \cos 2\varphi \pm Dk^2] \\ &\times [H_R + 4\pi M + \frac{2K_A}{M} \sin^2 \varphi - \frac{2K_U}{M} \pm Dk^2] \end{aligned} \quad . \qquad (45)$$

We plot the angular dependences of the resonance field of the FMR mode and their fitting (the solid lines) using Eq. (44) and (45) for the sample with 400 Å ferromagnetic layers of CoFe as Figure 4.3a and 4.3b. Figure 4.3(a) and 4.3(b) represent the configuration of the out-of-plane and the in-plane respectively. Below are the figures of the fittings:

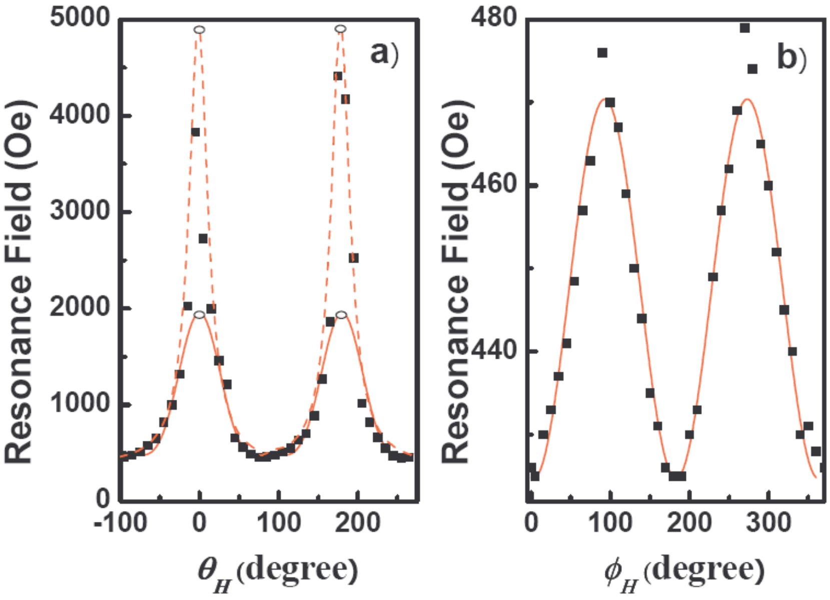

Fig. 4.3 Angular dependences of resonance fields of the FMR mode in both (a) the out-of-plane and (b) the in-plane configurations for the sample with 400 Å layers of CoFe. The solid lines show the fits using Eq. 44 and Eq. 45. The dashed line in (a) shows a new fit after compensating the surface and interface anisotropy into the free energy density. The resonant field at $\varphi_H = 0^o$ *is a singularity and cannot be reached.*

As evidenced by the nonsinusoidal shape of the angular dependence in Fig. 4.3(a) (out-of-plane configuration), we realized that the magnetic fields at which FMR is observed are not high enough to turn the magnetization vector M parallel to the magnetic field H when the latter has an out-of-plane component. We examined the equilibrium angles of the magnetization by minimizing the free energy density. The result is shown in Fig. 4.4.

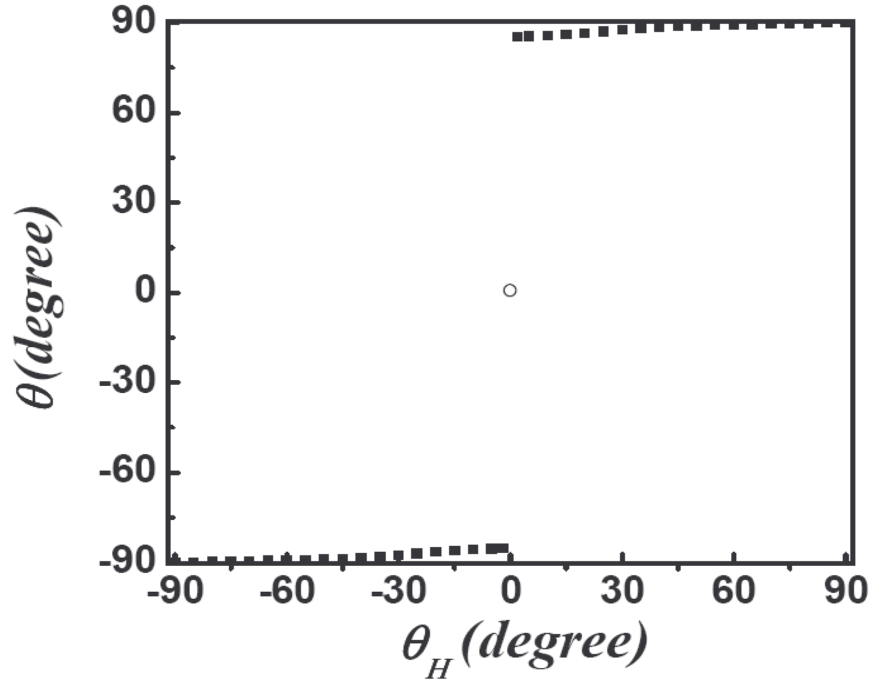

Fig. 4.4 Equilibrium angle of the magnetization as a function of angle of the applied field in the out-of-plane configuration ($\varphi_H = 0^o$).

It indicates that the direction of M immediately begins to seek the easy orientation as the magnetic field is tilted away from the direction normal to the sample surface (the resonant field at $\varphi_H = 0^o$ is a “singularity” and cannot be reached). In contrast to the out-of-plane configuration, the resonant magnetic fields are sufficiently high to turn the magnetization vector M parallel to the magnetic field H in the in-plane orientations. As shown in Fig. 4.3(b), a clear two-fold symmetry for the in-plane geometry corresponds to the uniaxial anisotropy field induced by the magnetic field annealing. We obtained the following parameters: γ= 1.835×1011 Hz/T, $4\pi M - \frac{2K_U}{M}$ = 2.4 T, and $\frac{2K_A}{M}$ ~ 50 Oe.

The values are consistent with those from our VSM measurements that give us a saturated magnetization of ~ 2.1 T and an in plane anisotropy of ~ 57 Oe. In the meantime, we notice that the experimental resonance data shows a strong deviation from the theoretical prediction in the out-of-plane configuration (Fig. 4.3a), particularly when external magnetic field, H is oriented close to the perpendicular direction of the film. The difference is attributed to the contribution of surface anisotropy.

4.2 Surface Magnetic Anisotropy and Dynamical Surface Pinning

It is well established that the interfacial and surface contributions are very important for analyzing the FMR field and linewidth of the magnetic trilayer structures [70-73]. As illustrated in Fig. 4.5, the broad feature at the high field side of the main mode can be deconvoluted a weak absorption line that is attributed to an exchange-dominated nonpropagating surface mode.

The surface mode disturbs the main resonance line and introduces an additional contribution of the FMR linewidth and an asymmetric line shape. Several groups have discussed the double peak feature in ferromagnetic samples in terms of the existence of surface uniaxial anisotropy [74]. For example, Teale et al. deduced that for parallel geometry the surface mode shifted from the bulk mode to higher fields with increasing positive values of the surface anisotropy constant corresponding to an easy-axis normal to the sample surface [75]. Wang et al. revealed that a negative contribution to the spin wave energy could be introduced by the surface anisotropy [76].

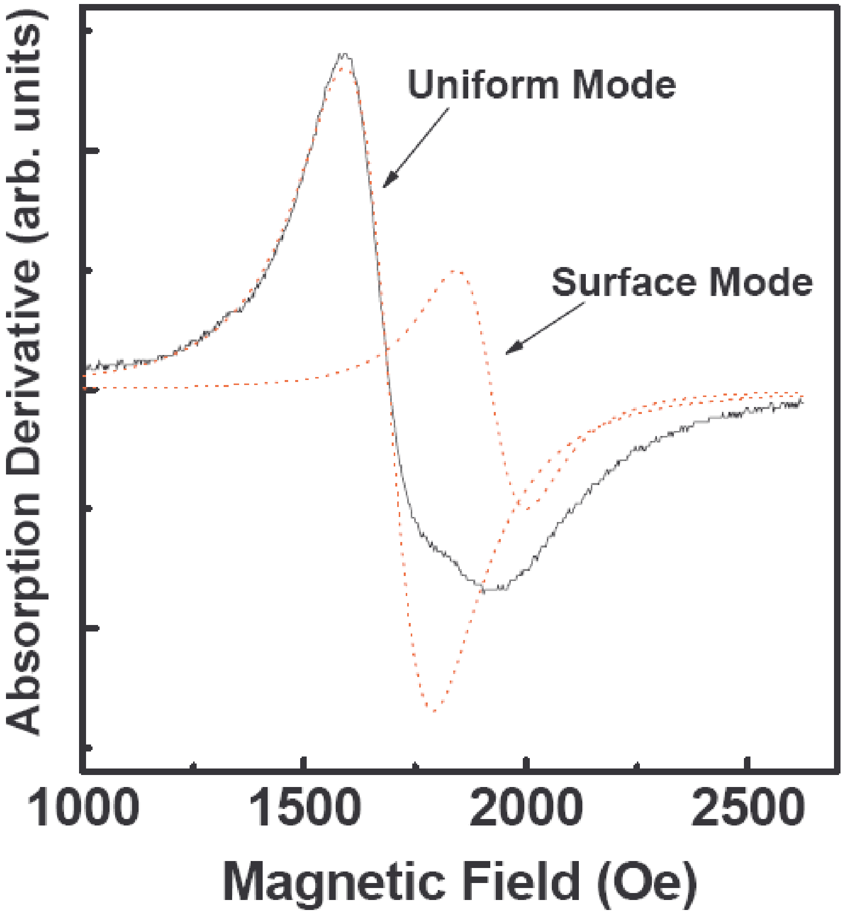

Fig. 4.5. A typical FMR spectrum observed in the sample with 400 Å layers of CoFe close to the out-of-plane magnetic field orientation. The dashed lines show the deconvolution of the spectrum indicating a uniform mode and a surface spin wave mode.

Here, we study the surface and interface properties of the trilayer samples by means of the surface spin wave and standing spin wave excitations. For a configuration close to out-of-plane ($\theta \sim 10^{o}$), in addition to a broad band feature on the high field side of the spectrum, which is attributed to an exchange-dominated nonpropagating surface mode, we have seen three FMR lines can be well resolved in the eight period *CoFe* trilayer structure as shown in Fig. 4.6.

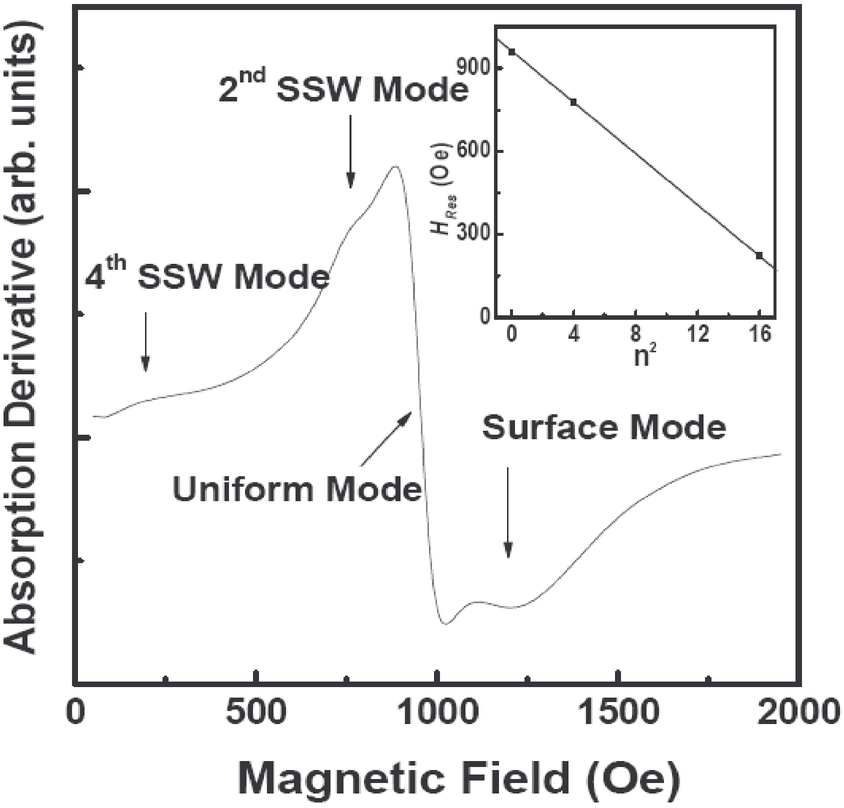

Fig. 4.6. A FMR spectrum in the eight period CoFe trilayer structure. The arrows show different spin wave modes. The inset shows a dependence of Hn measured at the out-of-plane configuration on the square of the corresponding mode number, n2. The line is a linear fit.

Figure 4.6 is a typical FMR resonance spectrum we got from the sample of NS02C which has an eight period trilayer structure with ferromagnetic layer thickness of 200 Å. This SWR spectrum consists of a main resonance line located at the highest field, with a series of weaker satellite peaks at lower fields. the strongest peak corresponds to the nonpropagating uniform mode (k = 0). We calculated the bulk magnetic anisotropy parameters and the g factor of the magnetic film based on the angle dependence of the main (strongest) resonance field. Additionally, two high-order standing spin wave modes were identified in our spectra corresponding to n=2 and n=4 spin wave modes.

The three FMR lines are identified as the uniform spin wave mode and high-order standing spin wave (SSW) modes. We analyzed the spin wave structure according to the change of the boundary conditions. In particular, as shown in the inset of Fig. 4.6, the positions of FMR lines for the sample are characterized by a mode separation that varies quadratically with n. This implies that spin precession of the spin waves at the surface is nearly free, which represents the so-called Kittel free boundary conditions, in which the position of the nth FMR line is given by Kittel Equation [77]:

$$H_n = H_0 - n^2 \frac{D}{g\mu_B} \frac{\pi^2}{L^2} \tag{46}$$

where H_0 is the position of the theoretical uniform mode, μ_B is the Bohr magnetron, n is an even integer (n = 0, 2, 4), and L is the total thickness of the *CoFe* layers. The observation of the high order even SSW modes in the eight period sample is due to the effective coupling between the *CoFe* layers. The antisymmetric modes (odd modes: n = 1, 3, 5) cannot be measured in our FMR technique, since in uniform thin films FMR selection rules allow only excitations with a net magnetic moment. The exchange stiffness D (which gives a measure of the strength of exchange interaction that tries to keep magnetic moments parallel) can then be determined from a linear fit shown in the inset of Fig. 4.6: D ~ 512 mev·Å^2, which can also be represented as D/gμB~ 42.03 T·nm^2.

Moreover, we realize that the separation between the uniform spin wave mode and standing spin wave mode depends strongly on the relative rotation angle θ with respect to the perpendicular direction of the film plate. As H is significantly rotated away from the normal, there is a critical orientation where only a single acoustic spin wave mode can be observed.

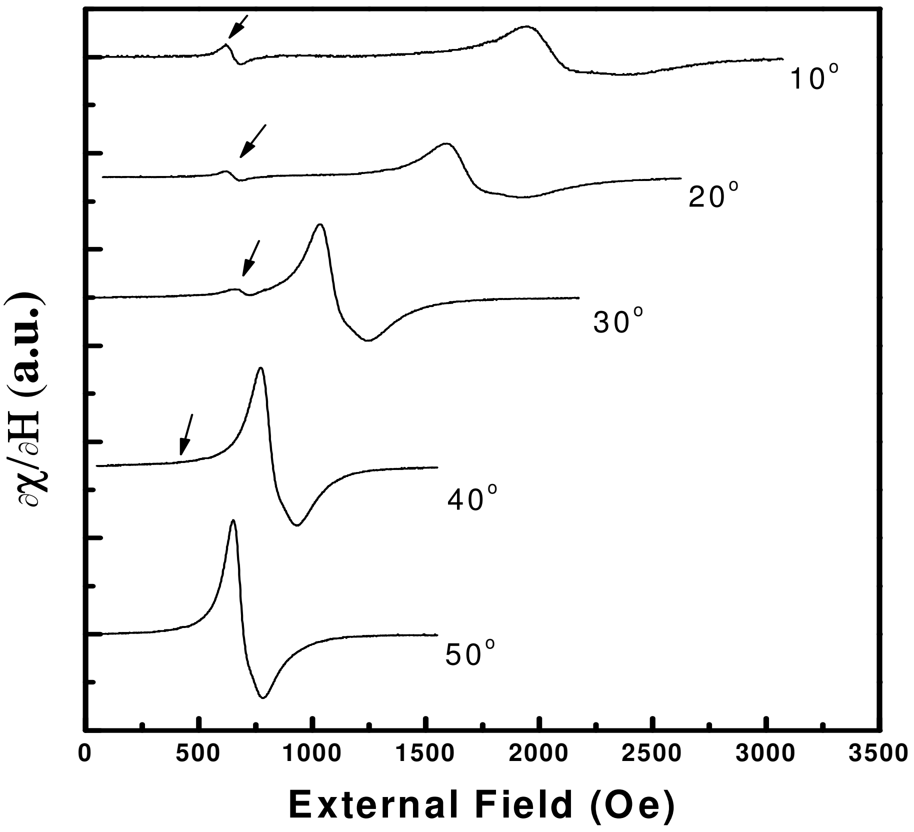

Fig. 4.7 SWR spectra for the single period of NS02A CoFe/PtMn/CoFe trilayer film (CoFe layer thickness 400 angstrom) at various orientation.

Fig. 4.7 illustrates spin-wave resonance (SWR) spectra for various magnetic field orientations of a tri-layer *CoFe* film. For a configuration close to out-of-plane ($\theta \sim 90^o$), in addition to a broad band feature on the high field side of the spectrum, which is attributed to an exchange-dominated non- propagating surface mode, two SWR lines can be well resolved. These lines are identified as the acoustic spin wave mode and high-order standing spin wave modes. As we rotate H away from $\theta = 0^o$, the high-order standing spin wave mode gradually loses its intensity. Eventually, at a critical angle, θ_C (~ 40^o) the multiple spin wave spectrum vanishes except for the single narrow resonance line due to the uniform spin wave excitation. We note that the complex behavior of angular dependence of the FMR spectrum described above shows some similarities to those previously reported in Permalloy [78,79], half-metallic ferromagnetic films [80], and recently in diluted magnetic semiconductors [81,82]. The results could be related to the change of surface spin pinning.

According to Puszkarski's surface inhomogeneity SI model, the actual eigenmodes are selected by the boundary conditions which in turn depend on dynamical surface spin pinning condition. We could include an effective surface anisotropy field (K_{surf}) to explain our results. Following the theory of surface states in FMR, the change of spin energy at each film surface and interface can be described by the effective parameter K_s discussed in Chapter 2.

The angular dependence of K_s can be used to qualitatively explain our angular dependent FMR spectra: As we rotate H away from the perpendicular direction of layer plane, K_s changes accordingly due to the change of the magnetization direction ($\vec{K}_{surf}$ is a constant vector). This leads to the change of surface boundary condition, which gives us a different value of the wave vector k. In turn, we will have a relative shift of FMR lines and relative intensity change between spin wave modes.

In addition, the uniform spin wave mode can also be shifted if we consider the contribution of the surface anisotropy field in the free energy density. As discussed by Puszkarski, the energy of all the spins present per unit area of the surface can be written as:

$$E_S = -\frac{Sg\mu_B}{d^2}(\vec{m} \bullet \vec{K}_{surf}) \qquad (47)$$

where S is the atom spin. Since $\vec{m}$ rotates with external magnetic field, we have E_S changing with the orientation of H.

Without considering surface effects, the experimental resonance data shows a large deviation from the theoretical prediction (fitting), particularly when H is oriented close to the perpendicular direction of the film. The dashed line in Fig. 4.3(a) shows a new fit after compensating the surface and interface anisotropy into the free energy density. The good fit of the experimental data obtained by including the surface energy reveals that we need to consider the energy contribution from the surface spin excitations. This is extremely important for designing magnetoelectronic devices based on nanoscale structures. In addition, as we can see from Eq. 4.6, the effective parameter *K* varies with changing angles when we rotate the sample, the magnetic profile changes due to the change of the surface pinning. This results in the change of the spin wave resonance energy.

Chapter 5

Time-Resolved Optical measurements

The application of ultrashort laser pulses was a major breakthrough in time resolved studies of magnetization dynamics, which extended time resolution into the sub-ps range. In fact, only time-resolved techniques can explore the magnetization dynamics down to the fs scale [83]. The all-optical pump-probe approach using the Kerr effect is one of the most applicable of these techniques, in which the ferromagnetic sample loses its ferromagnetic order due to the absorption of the laser pulse on timescales of 100fs [84].

Coherent oscillations associated with spin precessions can be observed in ultrafast optical experiments. The absorption of intense laser pulses by a ferromagnet causes a rearrangement of the electrons and the magnetic moments through fundamental microscopic physical processes, such as electron-electron scattering, electron-phonon scattering and magnon generation. All these processes are accessible with femtosecond laser pulses. With the time resolution inherent, femtosecond laser pulses in all-optical pump-probe experiments can be used to study the basic time constants of ultrafast demagnetization, the magnetic precessional modes, as well as the energy dissipation processes. We used the intensive 70fs laser pulses from a Ti:Sapphire oscillator with a wavelength of 800nm in the all-optical pump-probe scheme to investigate the magnetization dynamics of our thin ferromagnetic/antiferromagnetic/ferromagnetic trilayer structure and obtained good consistency with previous FMR studies on the same samples.

5.1 Time-resolved Pump-probe MOKE measurement

Time-resolved pump-probe optical spectroscopy based on ultrafast lasers is often used to study laser-induced transient-dynamics. The pump-probe technique uses a pump pulse to excite the sample, and a probe pulse to detect the sample relaxation. By varying the time delay relative to the pump pulse, time resolved measurements are possible. In an all-optical pump-probe scheme both the sample excitation and the detection of the relaxation process is done using laser pulses. Depending on the probe scheme, both the electron dynamics and magnetization dynamics can be recorded.

The pump-probe method triggers excitation in the initial status of the sample by using the pump beam pulse and, then, measures the final status with the probe beam pulse. An intense laser-pump pulse induces a fast perturbation of the material properties, the evolution of which can be studied through concomitant changes in the optical properties, as measured by a time-delayed probe pulse. In our experiments the probe pulse is derived from the pump, and delayed by a linear translation stage. To follow electron relaxation upon laser excitation, time resolved reflectivity of magneto-optical kerr effect is measured [85].

When the sample is hit by the pump beam, the intense pump-laser pulse strongly perturbs the ferromagnetic sample. The pump pulse energy enters the electron and phonon system, increases the thermal energy of the system and thereby the temperature of the sample [86]. The energy of the pump-laser pulse is transferred to the sample within the pulse duration of $\Delta\tau$ ~ 80fs. This causes an ultrafast demagnetization of the sample on timescales of < 1ps and triggers the coherent precession of the magnetization on the 100 ps timescale. The orientation of the effective magnetic field shifts and the magnetization aligns with the new easy axis for a couple of ps. The magnetization, already out of equilibrium, is not aligned with the effective magnetic field and starts to precess around the new easy axis with a tendency to align with the new effective field. The thermally induced anisotropy field pulse lasts no longer than a couple of ps until electrons, phonons and spins achieve thermal equilibrium [87]. Once thermal equilibrium is established, the easy axis of the ferromagnet returns back to the original position and the magnetization starts to precess around a constant effective field. The magnetic dynamical process is illustrated below:

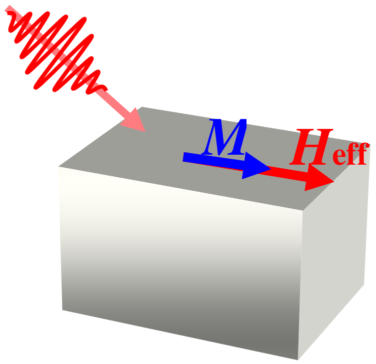

80fs Pump

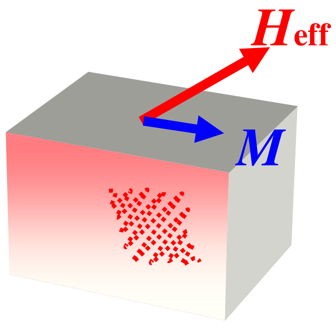

< 1 ps

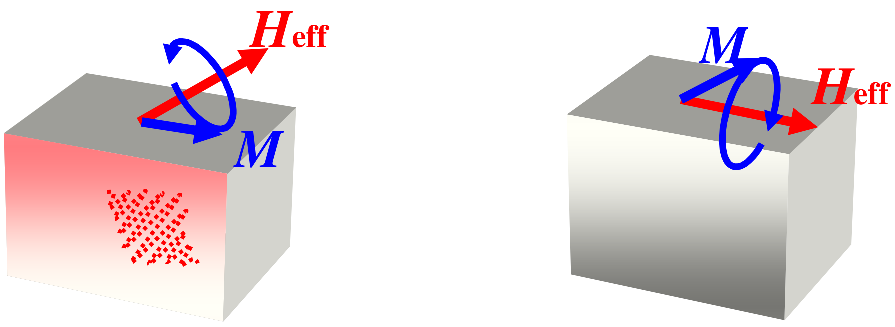

1 – 20 ps

<1 ns

Fig. 5.1 magnetic excitation in all-optical pump-probe experiments

Some magneto-optical phenomena are resulted from the direct action of the magnetic field on the orbital motion of the electrons, such as the Faraday effect (polarization change of the transmitted light) or magneto-circular dichroism (different absorption frequencies due to different polarizations). But Kerr effect (polarization change of reflected light) results from the direct spin-orbit coupling, and can be described as a change in the polarization of light reflected from a magnetic sample proportional to the internal magnetization in the sample itself [88]. It originates from different optical absorption coefficients of the material for left and right circularly polarized light. For the longitudinal Kerr effect H is applied in the film plane and in the plane of the incident light, making it sensitive to the in-plane component of the magnetization.

The optical response of the material is described by a dielectric tensor ε which can be decomposed into symmetric and anti-symmetric parts [89]. The normal modes of the symmetric part of ε are left and right linearly polarized light, which do not contribute to the magneto-optical effects.

Therefore, without losing generality, only the dielectric tensor for the isotropic materials is considered:

$$\varepsilon = \varepsilon_{xx} \begin{pmatrix} 1 & -iQm_z & iQm_y \\ iQm_z & 1 & -iQm_x \\ -iQm_y & iQm_x & 1 \end{pmatrix} \tag{48}$$

where Q = $i\dfrac{\varepsilon_{xy}}{\varepsilon_{xx}}$, is the magneto-optical constant, and m =(m_x, m_y ,m_z) is the unit vector of the magnetization vector M. The normal modes of ε are left and right circularly polarized light, with eigenvalues ε_L and ε_R, given by

$$\begin{aligned} \varepsilon_L &= 1 - Qm \cdot k \\ \varepsilon_R &= 1 + Qm \cdot k \end{aligned} \tag{49}$$

The non-zero difference between those eigenvalues contributes to magneto-optical effects such as the polarization change of the reflected light from the ferromagnet [90]. The expression for the Kerr effect is derived from the Fresnel reflection matrix R, whose off-diagonal terms originate from spin-orbit coupling. In the basis of p and s polarized light, the Fresnel matrix is expressed as:

$$R = \begin{pmatrix} r_{pp} & r_{ps} \\ r_{sp} & r_{ss} \end{pmatrix} \tag{50}$$

The complex Kerr angle Θ_K for p and s polarized light is defined by;

$$\Theta_K^S = \theta_K^S + i\varepsilon_K^S = \frac{r_{ps}}{r_{ss}}$$
$$\Theta_K^P = \theta_K^P + i\varepsilon_K^P = \frac{r_{sp}}{r_{pp}} \qquad (51)$$

5.2 Broad-band Ferromagnetic Resonance and Relaxation in the Ferromagnetic Multilayer Films

The pump-probe differential magnetic Kerr (DMK) experiments in the *FeCo16* trilayer structures were performed at in the Voigt geometry using a *Ti*-sapphire laser that provided ~ 70 fs pulses of central wavelength 800 nm at the repetition rate of 80 MHz. The pump pulses induce coherent magnetic precessions modifying the reflection of the probe pulses that follow behind. Time-domain DMK measurements give the pump-induced shift of the polarization angle of the reflected probe field, $\Delta\theta$, as a function of the time delay between the two pulses [91].

We conducted experiments for various external magnetic fields at both room temperatures and low temperature (about 77 k). The output power of the pump laser beam we used was about 400mw and probe power was about 150mw. Below is the DMK data for the sample with *CoFe* layer thickness of 200 Å. From Fig. 5.2, we can clearly see the typical time-resolved MOKE spectrum. The strong negative peak shortly after the pump pulse reaches the sample represents an ultrafast demagnetization which indicates "time zero", the zero phase difference between pump and probe laser beams. For higher external magnetic fields, we observed oscillations with higher frequencies and more complicated modes.

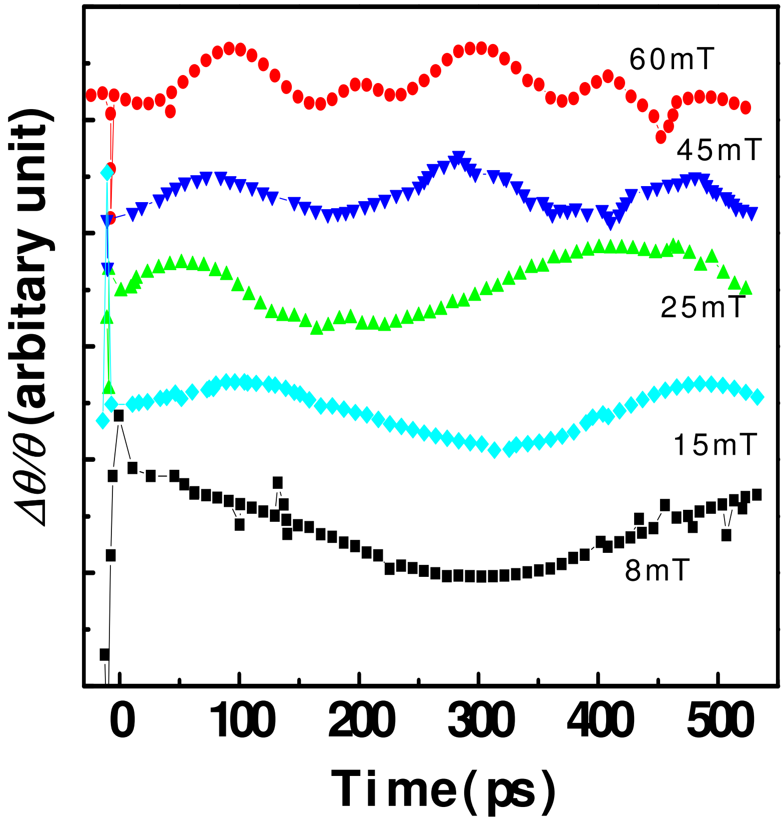

Fig. 5.2: Pump-probe MOKE oscillation under different magnetic fields in sample with CoFe layer thickness of 200 Å. (fields are indicated by the currents operated in electromagnets.

The oscillations are assigned to the precession of the magnetization around M_0. We used linear prediction methods to fit the 320-Oe time-domain data. As shown in the inset of Fig. 5.3, the Fourier transform of the fit reveals three modes, which are assigned to S_E, S_0, and S_D. While S_E and S_0 refer to the surface and bulk exchange-dominated spin wave modes, the observation of S_D, the non-homogeneous dipole mode is due to the finite penetration depth of the pump pulses. The three modes were observed in the DMK spectra of all the samples and show little dependence of thickness of the samples. The frequencies of the modes are plotted as a function of the applied magnetic field in Fig. 5.4, together with FMR results for the 200-Å sample.

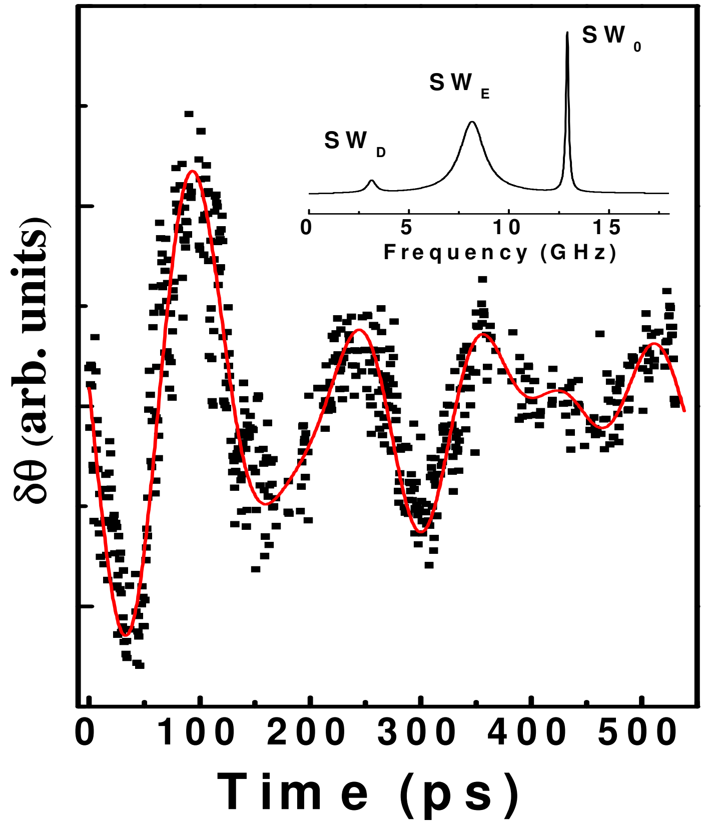

Fig. 5.3 Voigt-geometry DMK data for the 20-nm CoFe/PtMn/CoFe film (solid square) at H_0 = 320 Oe. The red curve is the linear prediction fit. The inset shows the Fourier transform of the fit.

Magnetization relaxation after intensive pump-laser pulse excitation is followed by ultrafast demagnetization, which happens shortly after the pump laser reaches the sample, and by the coherent and incoherent collective relaxation modes, which happen on the ns time scale. The main characteristics of both coherent and incoherent relaxation processes are first introduced on different samples by varying the external field amplitude. Different precession modes appear to depend on the thickness of the ferromagnetic sample. For FM layer thickness much smaller than optical penetration depth, the basic Kittel mode is the dominant relaxation mode and is governed by the external magnetic field. In our case, the FM thickness is comparable to the penetration depth (~ 20nm), we can see both homogeneous and inhomogeneous modes. For FM layer thickness is much larger than the penetration depth, the inhomogeneous dipole mode shows its relative significance. Dipole dominated modes are observed for films considerably thicker than the optical penetration depth. These modes are present even without an external field.

The coherent magnetization processes are characterized by the correlated behavior of the atomic magnetic moments. The neighbor spins do not relax independently in the local effective magnetic field. Rather the exchange correlation between them causes the coherent behavior observed in the time resolved magnetization relaxation spectrum [93]. The precession modes are characterized by the precession frequency $\omega = 2\pi\nu$ and the Gilbert damping parameter α, which describes the timescale on which the magnetization aligns with the effective magnetic field.

In all-optical pump-probe experiments, the magnetization, disturbed from equilibrium by the intensive laser pulse, begins to precess in the effective magnetic field. Only the sample surface within the optical penetration depth λ_{opt} is directly excited by the pump-laser pulse. The various magnetic precession modes are triggered in samples with different ferromagnetic layer thicknesses. These modes can be classified by their origin into those led by the external magnetic field, by the exchange field and by the dipole field in the sample itself.

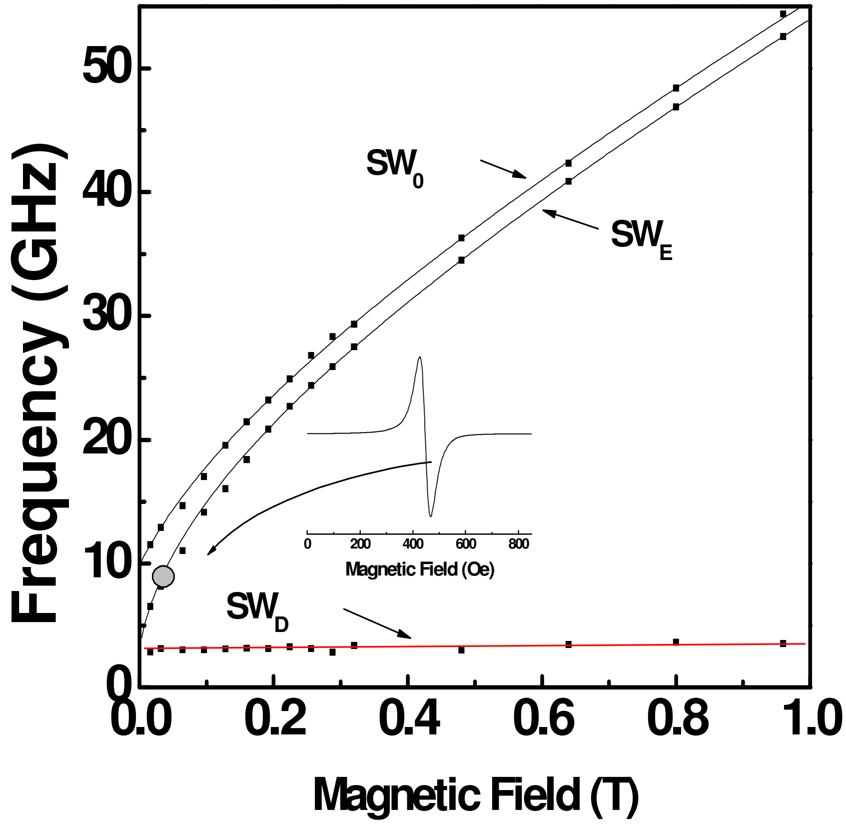

Fig. 5.4: Measured magnetic-field dependence of the precession mode frequencies. The inset is the FMR spectrum and the solid lines show the fits.

We investigated the dispersion relation of those three modes in external field amplitude dependence for our samples. The time resolved MOKE spectra can be directly analyzed in the time regime and also in the frequency regime using the Fourier transformations. Fitting the time resolved spectra to the damped sine function gives access to timescales of magnetization precession and magnetization torque energy dissipation.

By increasing the external magnetic field amplitude, both amplitude and frequency of the magnetic precession increase. The external magnetic field shifts the direction of the effective field further out of plane, which is opposite to the tendencies of the demagnetization and anisotropy field to keep the magnetization in the plane. The precession mode, which dominates the magnetization relaxation for this sample, is a volume homogenous coherent mode, which is often called the basic mode or Kittel mode. Here, the spins are aligned parallel to each other and there is no phase shift between the neighbor spins, which means that this mode can be characterized with the wavevector k = 0, due to the formalism of the spin waves.

From analysis of Fig. 5.3 and Fig. 5.4, we can clearly find out, increasing the amplitude of the external field enhances both the precession frequency and amplitude. The precession amplitude of the basic k = 0 mode is significantly larger than that for higher oscillation, which implies that the Kittel mode is the dominant coherent channel for the magnetization relaxation.

The additional precession modes can be attributed to the surface spin wave modes (SSW). The wave vector of the surface spin waves align with the surface. The surface modes perform wavelike behavior on the surface but its amplitude attenuate in the bulk. The standing spin-wave mode forms if the film thickness is larger than the optical penetration depth λ_{opt}. The standing first order spin-wave modes have been observed previously in time resolved pump-probe experiments by van Kampen *et al*. This study determined the dispersion relation of PSSW in regard to the thickness of the ferromagnetic layer [94]. Due to the exchange interaction between spins given by the constant D, the frequency of the standing spin wave mode ν_1 is higher than the frequency of the basic mode ν_0:

$$\nu_1 = \nu_0 + Dk^2\ ,\ \ k = \pi/d\ . \tag{52}$$

The wave vector k of the PSSW can be determined by defining the boundary conditions at the sample surface and the interface with the substrate. Boundary conditions are defined by pinning the spins at the interfaces. For strong surface anisotropy fields, spins at the interface are fixed and the fixed boundary conditions are applied. In our case, however, the clear observation of surface mode indicates that the surface and interface effect are nontrivial and might be crucial in the magnetic excitation process of ferromagnetic multilayer thin films.

5.3 The coupling between magnetic precession and optical pulses

The Kerr effect can be described as a change in the polarization of light reflected from a magnetic sample proportional to the internal magnetization in the sample itself. It originates from different optical absorption coefficients of the material for left and right circularly polarized light.

The coupling between magnetic precessions and probe pulses is controlled by the antisymmetric spin-flip Raman susceptibility, which is closely related to that for Faraday rotation [95]. Raman selection rules were found to be strictly obeyed in all cases. In our Voigt geometry, the scattered probe field associated with m_y component of the precession is polarized along the z axis and, therefore, gives no DMK signal. Using results for scattering by coherent vibrations, we get for m_z scattering

$$(\nabla^2 - \frac{n_R^2}{c^2}\frac{\partial^2}{\partial t^2})(e_x \pm ie_y) = \frac{4\pi\chi_M}{c^2}\frac{\partial^2}{\partial t^2}[m_z(z,t)(e_y \pm ie_x)] \tag{53}$$

where e=(e_x ,e_y,0) is the probe electric field, n_R is the refractive index, $\chi_M = \partial \chi^{(0)}/\partial M$, and $\chi^{(0)}$ is the linear susceptibility. Let us define the average

$$\langle m_Z(t)\rangle = (1/L)\int_{-L/2}^{+L/2} m_Z(z,t)\,dz \ . \tag{54}$$

To lowest order, and provided (i) $Ln_R/c \ll 2\pi/\Omega$ and (ii) multiple reflections can be ignored (these assumptions are well obeyed in our experiments). If we only consider the homogenous spin wave excitations here, the coherent scattering is equivalent to a slowly varying modulation of the refractive index,

$$\delta n_R(t) = \pm(2\pi\chi_M / n_R)\langle m_z(t)\rangle , \tag{55}$$

with different signs for the two senses of circular polarization [96]. Except for the constant factors, this expression is identical to that describing FMR. Because $\langle m_Z(t)\rangle$ vanishes for odd precessions, Eq. (55) supports our contention that the two modes observed in the experimental data are S_0 and S_E.

We describe our data by the Landau-Lifshitz equation of motion for the magnetization M. The eigen-frequencies of the magnetization procession are

$$\begin{aligned}\omega^2 &= \gamma^2\left[H_0 + \frac{2K_A}{M_0}\right][H_0 + 4\pi M_0 + 2M_0^{-1}(K_A - K_U)] \\ &\pm DK^2\gamma^2[(H_0 + \frac{2K_A}{M_0}) + (H_0 + 4\pi M_0 + 2M_0^{-1}(K_A - K_U))] + \gamma^2 DK^2\end{aligned} \tag{56}$$

where the plus (minus) sign corresponds to the bulk-(surface-) like modes, K_U and K_A are the out-of-plane and in-plane anisotropy constants. The eigenmodes are selected by the conditions at the boundaries [51]:

$$\frac{\partial m_y}{\partial z} = 0\,,\ \frac{\partial \ln m_z}{\partial z} = -2K_S / DM_0,\ \text{and}\ \frac{\partial \ln m_z}{\partial z} = 2K_f / DM_0\ \text{at } z=\pm L/2, \qquad (57)$$

where K_S and K_f are the surface and interface anisotropy constants that can be determined by the ratio between the amplitudes of S_E and S_0. Here we neglect the exchange bias field between the *CoFe* layer and the *PtMn* layer according to the VSM hysteresis results on the *CoFe/PtMn/CoFe* samples. The interlayer exchange interaction between the *CoFe* layers is small due to their large separation.

Unlike the sharp selection rules of Raman type observed in probe scattering [97], we found that the strength of the oscillations is nearly the same for pump pulses of arbitrary circular or linear polarization. The results point towards a relatively simple thermal origin relying on the temperature dependence of the anisotropy [98]. A sudden deviation of the orientation of M_0 is due to the temperature rise that follows the absorption of the light pulse. The easy-axis orientation moves to a new orientation after the pulse hits. The solid line in Fig 5.3 shows the fitting of the present DMK data using the above equation [99].

From the fitting, we obtained: g = 2.01, the out-of-plane uniaxial anisotropy, $2K_U/M \sim 0.3$ T, the effective in-plane anisotropy, $2K_A/M \sim 0.01$ T, the effective demagnetization field, $4\pi M_{eff} \sim 2.4$ T and the spin stiffness, $D \sim 451$ meV.Å^2. Our values for the bulk anisotropy are in fairly good agreement with the VSM measurements. The time-resolved MOKE experiment provides an effective method for studying spin dynamics of multilayer magnetic structures. The surface anisotropy contribution is found to be critical for understanding the magnetization dynamics.

Chapter 6

Spin Wave Relaxation Dynamics

In addition to the ferromagnetic resonant field, another important parameter in the application of microwave magnetic materials is magnetization relaxation (also called damping). The parameter is closely related to the FMR linewidth of the materials. Damping is the dissipation of vibration energy and the consequent reduction or decay of motion. Magnetization damping in thin ferromagnetic films plays a crucial role in application because of its importance for the switching of fast spintronic devices.

The magnetization, disturbed from equilibrium by an intensive laser pulse, precesses around a magnetic field H and tries to align with it on timescale τ_α, given by the macroscopic damping parameter *α*. The magnetization vector obeys the Landau-Lifshitz equation of motion:

$$\frac{dM}{dt} = -\gamma M \times H + \frac{\alpha}{M_S} M \times \frac{dM}{dt} \qquad (58)$$

with a Gilbert form of damping. α is the damping constant (with no dimension). On the right side of Eq. (58), the first term (azimuthal component) corresponds to undamped precession and the second term corresponds to the "damping torque" TD, which makes M_S move towards the direction of H_{eff}.

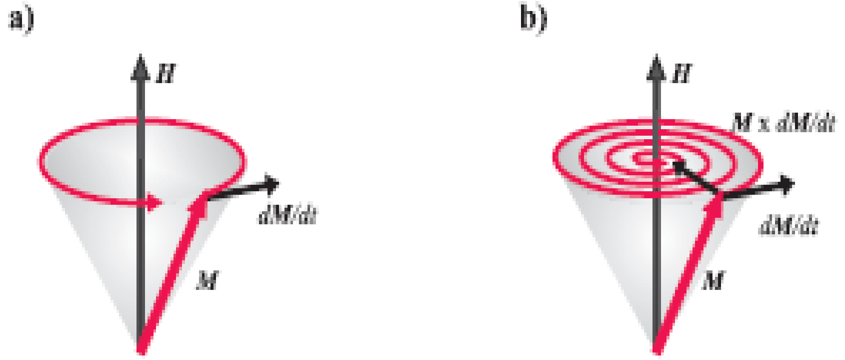

Figure 6.1: The precession of Ms (a) without damping (Larmor precession); (b) with damping.

The damping can be classified by the direction of energy transfer into indirect and direct. If energy is conserved within the magnetic system and redistributed between different magnetic degrees of freedom, the damping is indirect. Damping of spin waves by Stoner excitations and mode conversions are examples of indirect damping [100]. Direct damping specifies the transfer of energy from the magnetic system to the other nonmagnetic degrees of freedom, mainly the lattice. It originates from spin-orbit coupling, and can be classified into *intrinsic* damping, always present in a particular material, and *extrinsic* damping, which can be suppressed through control of microstructure.

6.1 Intrinsic damping

At finite temperature, the scattering of spin waves (magnetic excitations) with electrons and phonons is an integral part of the system. These processes are called intrinsic. Intrinsic damping, also called as Gilbert damping, is a material characteristic and cannot be reduced. It comes from unavoidable contributions intrinsically inherited by the material. For example, at finite temperatures collisions between phonons and magnons can not be avoided. The magnetic relaxation processes which involve the electron scattering with phonons and thermally excited magnons are intrinsic dampings. The intrinsic FMR linewidth can be derived from the free energy density E [101]:

$$\Delta H_{in} = \frac{2}{\sqrt{3}} \bullet \frac{1}{\left|\frac{\partial \omega}{\partial H_{res}}\right|} \bullet \frac{\alpha\gamma}{M} \left(\frac{\partial^2 E}{\partial \theta^2} + \frac{1}{\sin^2 \theta} \bullet \frac{\partial^2 E}{\partial \phi^2}\right). \tag{59}$$

There are three major mechanism which can cause intrinsic damping in metallic ferromagnets: eddy current, magnon-phonon coupling and itinerant electron relaxation, but in the limit of ultrathin ferromagnetic films, the itinerant nature of electrons and spin-orbit interaction plays a dominant role. Thus the mechanism of intrinsic damping in ferromagnetic thin films can be described as spin-flip and spin-conserve collision between mobile electrons and magnons, incoherent scattering of electron-hole pair excitations by phonons and magnons, and direct magnon-phonon interaction.

Intrinsic magnetic relaxation in metals is caused by incoherent scattering of electron-hole pair excitations by phonons and magnons. The electron-hole interactions involve three particle scattering. The excitations are either accompanied by electron spin flip or the spin remains unchanged. Spin-flip excitations can be caused by the exchange interaction between magnons and itinerant electrons (s-d exchange interaction), during which the total angular momentum is conserved [102]. The spin conserving scattering is caused by spin-orbit interaction which leads to a dynamic redistribution of electrons in the electron k-momentum space. The Gilbert damping can be calculated using Fermi's golden rule, which sums up all available states that satisfy the energy conservation.

We investigate the magnetization damping from the FMR linewidths in these trilayer structures and plot the angular dependence of the linewidth (from peak to peak of the differentiated signal).

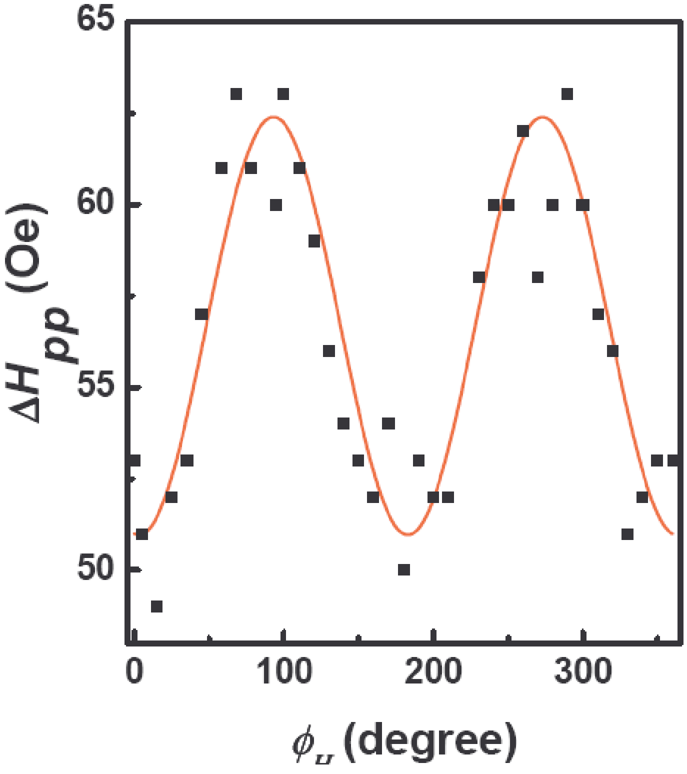

Fig. 6.2: FMR linewidth as a function of in-plane angle between the applied field and the easy axis for the sample with 400 Å layers of CoFe.

Figure. 6.2 illustrates the FMR linewidth as a function of the in-plane angle between the applied field and the easy axis in the sample with 400 Å layers of *CoFe*. The solid line shows a fit by using Eq. (59). The good consistency between the experimental data and the fitting shows that our measured resonance linewidth, ΔH_{pp}, is mostly governed by the phenomenological Gilbert damping. We calculate the Gilbert damping parameter α according to above equation. We obtain $\alpha = 0.012 \pm 0.002$. The parameter α is not thickness dependent and does not depend on the resonance frequency as well. This behavior agrees with the nature of the Gilbert damping.

6.2 Extrinsic Damping

In experiments, the linewidth is also found to have linear frequency dependence with an extrapolated non-zero linewidth with zero frequency $\Delta H(0)$ [103]. Consequently, the measured linewidth versus frequency is often interpreted by a simple relation:

$$\Delta H(\omega) = \Delta H(0) + \alpha \frac{\omega}{\gamma} \quad , \qquad (60)$$

where the linear term is assumed to be a measure of intrinsic damping and $\Delta H(0)$ depends on film quality and approaches zero for perfect sample. This implies $\Delta H(0)$ is extrinsic and caused by structural or compositional defects. And they are labeled as extrinsic contribution.

Previous studies of FMR linewidth in magnetic materials showed that the dependence of the FMR linewidth on the microwave frequency follows a linear dependence [104]:

$$\Delta H = \Delta H_{ex} + 1.16 \frac{\omega}{\gamma} \frac{G}{\gamma M_s} \qquad (61)$$

from which the Gilbert damping parameter can be determined. ΔH_{ex} is the frequency independent linewidth which arises from the presence of magnetic inhomogeneities, thus it is contribution of extrinsic damping.

For the FMR linewidths in the trilayer structures discussed in last section, the measured resonance linewidth ΔH_{pp} is the sum of the intrinsic Gilbert damping contribution ΔH_{in} and extrinsic inhomogeneous line broadening ΔH_{ex}. Extrinsic scattering can vary from one sample to another, depending upon preparation. It arises from microstructural imperfections or finite geometry. It can, at least in principle, be suppressed. Intrinsic scattering is present for a perfect single crystal at a given temperature; it comes about mostly through interaction with lattice vibrations (phonons). Intrinsic scattering cannot be suppressed.

6.2.1 Two magnon scattering

The inhomogeneous linewidth broadening, which is caused by magnetic inhomogeneities in the sample, is due to extrinsic damping. These inhomogeneities come from structural defects and complex geometrical features in the sample and they can in principle be avoided. Two-magnon scattering is a significant source of relaxation in materials containing magnetic inhomogeneities. Surface roughness, grain boundaries and atomic disorder are potentially important sources of the scattering. The basic idea is that such inhomogeneities results in a coupling between the otherwise orthogonal uniform precession and degenerate spin-wave modes and that energy transfer out of the uniform precession to the degenerate modes is important in the initial stages of relaxation [105]. The total number of magnons is unchanged since one magnon is annihilated and another is created. The interaction is sensitive to the nature of the inhomogeneity. As a general rule, the coupling is large for spin-wave wavelengths greater than the dimensions of the inhomogeneity.

In the idealized FMR experiment, a uniform mode is excited whose wave vector $k_{//}$ parallel to the surface is zero. In the presence of dipolar couplings between spins, there will be short wavelength spin waves degenerate with the FMR mode. Defects in the film scatter energy from the uniform modes to these states, producing relaxation of dephasing character.

In two magnon scattering the magnon momentum is not conserved due to sample inhomogeneities (loss of translational invariance), but the energy is conserved. The two magnon scattering eventually decreases linearly to zero with decreasing microwave frequency. For both 2D and 3D spin-wave manifold there are no magnons degenerate with the FMR mode in the perpendicular configuration, hence the FMR linewidth should be smaller than that in the parallel configuration [106]. A convincing evidence for two magnon scattering mechanism was obtained by investigating the dependence of FMR linewidth on the angle µH between the dc magnetic field and the sample plane. When the magnetization is inclined from the surface, the damping decreases significantly. The calculated FMR linewidth takes the intrinsic value of the Gilbert damping. The difference between the measured FMR linewidth and that expected for the intrinsic damping is caused by two magnon scattering. The peak in the FMR linewidth is caused by dragging of the magnetization behind the external applied field.

Most recently, Rezende *et al.* deduced that the spin-wave relaxation rates measured by FMR can be fitted with a t^{-2} dependence plus a constant term if one includes both the intrinsic mechanism dominated by the Gilbert damping and the extrinsic mechanism dominated by the two-magnon scattering [107]. According to Arias-Mills theory, Δf_{res} can be related to the local interfacial exchange energy J_I,

$$\Delta f_{res} \propto \left(\frac{J_I}{K_s t}\right)^2 \Rightarrow \Delta f_{res} \propto t^{-2} \qquad (62)$$

Based on theory of two magnon scattering, we investigated the relationship between the FMR linewidth and the thickness of ferromagnetic layer. Fig. 6.3 shows FMR linewidth versus FM layer thickness and the fitting of t^{-2} is plotted.

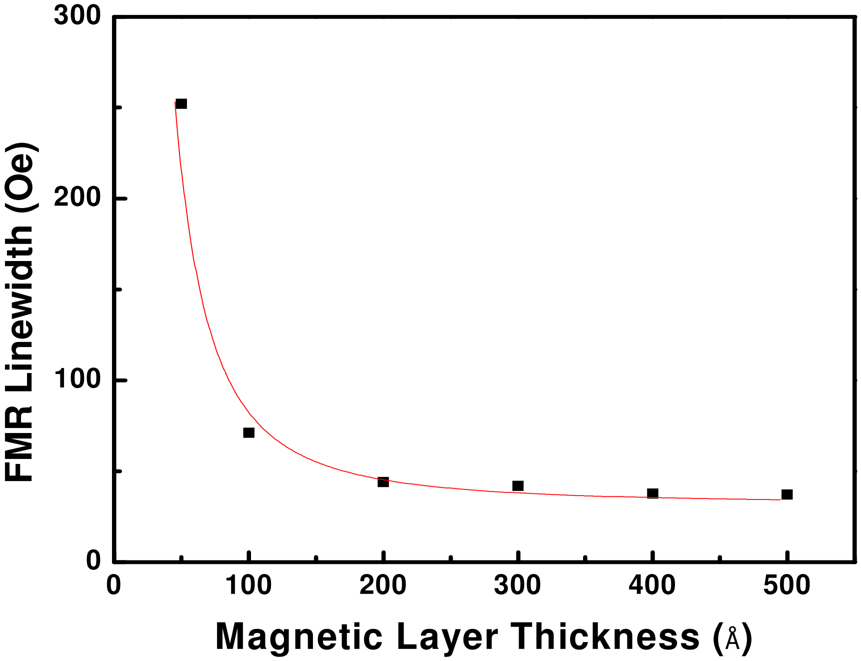

Fig. 6.3: t^{-2} fitting of linewidth vs. ferromagnetic for NS series CoFe16 Ru-seeded FM/AFM/FM trilayer sample.

In addition to the intrinsic mechanism in the damping parameter, we also see an extrinsic contribution on the spin relaxation dynamics when we further measured the FMR linewidths of samples with thinner layers of *CoFe*. The extrinsic contribution generally includes two-magnon scattering and so-called inhomogeneous linewidth broadening caused by nonuniformities of the magnetic properties in the measured volume [108]. Here, we neglect the influence of linewidth broadening due to locally nonuniform material properties since $H_{res} \geqslant 500$ Oe outweighing the varying anisotropic field of about millitesla range in the trilayer samples [109]. While the intrinsic linewidth ΔH_{in} does not depend on the resonance frequency at fields H_{res}, the two-magnon scattering due to fluctuations of the interlayer exchange coupling showed a strong thickness dependence of the FM layers with t^{-2} relation as we can see it from Fig. 6.4.

Although the fitting of t^{-2} for the linewidth vs. FM layer thickness is very good for layer thinner than 400 Å, we noticed small discrepancies for the 400 Å and 500 Å samples. In order to understand the linewidth broadening caused by extrinsic damping comprehensively, we conducted further investigation.

6.2.2 Surface and interface effect in relaxation

We use t^{-2} dependence to estimate the contribution from the two-magnon scattering by studying the linewidths of *CoFe* trilayer samples with various thicknesses of the ferromagnetic *CoFe* layers. Fig. 6.4 shows the FMR linewidth (ΔH_{pp}) as a function of the thickness t of FM layers in two *CoFe* trilayer sample series grown with seed layers of *Ru* and *NiFeCr*, separately. The magnetic field is applied along their easy axis direction. We fit the data by the t^{-2} dependence shown as solid lines. The consistency between the fitting and experimental results indicates an extrinsic origin, dominated by two-magnon scattering processes.

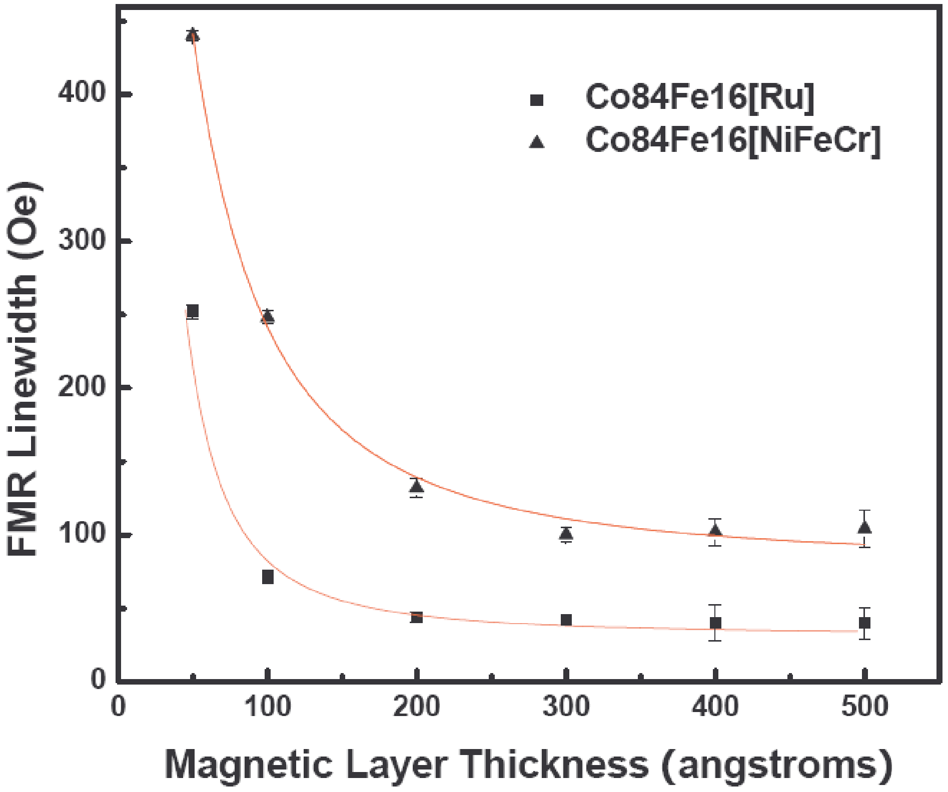

Fig. 6.4: FMR linewidth (ΔHpp) as a function of the thickness t of FM layers in two CoFe trilayer sample series grown with seed layers of Ru and NiFeCr. The solid lines are the t^{-2} *fits.*

But in the meantime, comparing to that of the *Ru*-seeded samples, we noticed a significant linewidth broadening in the *NiFeCr*-seeded *CoFe* layers. Since as the *Ru* seed layers were replaced by *NiFeCr*, only the interface properties were modified, our result shows that the surface and interface properties of multilayer structures are crucial for understanding the spin wave resonance and the processes of spin wave relaxation. We conducted extensive data analysis for FMR linewidths of our samples and also did investigation on this topic using both FMR and Pump-probe MOKE techniques. Our results indicated clearly that the interface exchange interaction and surface effect play important role particularly in the linewidth of samples with thicker ferromagnetic layer.

Chapter 7

Summary

Using both frequency and time domain measurement techniques, we investigated the magnetic dynamical properties including magnetic anisotropies, Gilbert damping, two-magnon scattering, and effective magnetization in a series of multilayer *CoFe/PtMn/CoFe* films grown on the seed layer *Ru* and *NiFeCr* with *CoFe* compositions being *Co-16* at. *%* Fe.

The FMR measurements were taken for samples with the ferromagnetic *CoFe* layer thicknesses varying from 10 Å to 500 Å. The magnetic anisotropic parameters were determined by rotating the field aligned axis with respect to the spectral field in the configurations of both in-plane and out-of-plane. We calculated and obtained the unidirectional in-plane anisotropic parameter $\frac{2K_A}{M}$ ~ 0.005 T, an effective magnetization of $4\pi M - \frac{2K_U}{M}$ ~ 2.4 T, and the exchange stiffness D ~ 512 meV · 400 $Å^2$. Moreover, the measured resonance linewidth of *CoFe/PtMn/CoFe* were analyzed by the thickness dependence of the *CoFe* layers.

We also performed pump-probe differential magnetic Kerr (DMK) experiments in the trilayer structures in the Voigt geometry using a Ti-sapphire laser that provided ~ 70 fs pulses of central wavelength 800 nm at the repetition rate of 80 MHz. The pump pulses induce coherent magnetic precessions modifying the reflection of the probe pulses that follow behind. Time-domain DMK measurements give the pump-induced shift of the polarization angle of the reflected probe field, $\Delta\theta$, as a function of the time delay between the two pulses. We observed clear pump-probe MOKE oscillations and Fourier transform of the fitting reveals three modes, which correspond to the surface and bulk exchange-dominated spin wave modes, and the dipole mode. The observation of S_D, the non-homogeneous dipole mode is due to the finite penetration depth of the pump pulses. The three modes were observed in the DMK spectra of all the samples and show little dependence of thickness of the samples. Our results of time-domain measurements showed good consistency with FMR measurement.

We conclude that the spin wave relaxation could be described in terms of two independent contributions: they are the intrinsic mechanism dominated by Gilbert damping and the extrinsic mechanism dominated by two-magnon scattering. Finally, we reveal that a significant linewidth broadening could also be caused by the overlap of the surface and the uniform spin wave modes. The surface anisotropy energy has been revealed to be critical for understanding the FMR lines.

Bibliography:

1. N. Saleh and A.H. Qureshi. Electron. Lett. 6 (1970).
2. Y. Lamy and B. Viala, J. Appl. Phys., vol. 97, , (2005)
3. Y. Lamy and B. Viala, IEEE Trans. Magn., vol. 41, no. 10, (2005)
4. Mark J. Jackson , Microfabrication and Nanomanufacturing, Published by CRC Press, (2006)
5. Pettiford, C.; Zeltser, A.; Yoon, S.D.; Harris, V.G.; Vittoria, C.; Sun, N.X. Magnetics, IEEE Transactions on Volume 42, Issue 10, (2006)
6. C.I. Pettiford, A. Zeltser, S.D Yoon, V.G. Harris, C. Vittoria, and N.X. Sun, J. Appl. Phys. 99, 08C901 (2006)
7. B. Skubic, E. Holmström, D. Iusan, O. Bengone, O. Eriksson, R. Brucas, B. Hjörvarsson, V. Stanciu, and P. Nordblad, Phys. Rev. Lett. 96, 057205 (2006)
8. N.T. Thanha, b, M.G. Chunb, N.D. Haa, K.Y. Kimb, Journal of magnetism and magnetic materials, vol. 305, (2006)
9. B. Kuanr Z. Celinski, R. E. Camley. Appl. Phys. Lett. 83, 3969 (2003).
10. B. Kuanr D. L. Marvin, T. M. Christensen, R. E. Camley, Z. Celinski. Appl. Phys. Lett. 87, 222506 (2005).
11. M. Yamaguchi, S. Arakawa, H. Ohzeki, Y. Hayashi, K. I. Arai, IEEE Trans. Magn. 28,3015 (1992).

12. A. M. Crawford, D. Gardner, S. X. Wang, IEEE Trans. Magn. 38, 3168 (2002).
13. B. Viala, A. S. Royet, R. Cuchet, M. Aid, P. Gaud, O. Valls, M. Ledieu, O. Acher,IEEE Trans. Magn. 40, 1999 (2004).
14. H. S. Jung, W. D. Doyle, and H. Fujiwara, “Exchange coupling in FeTaN/IrMn/FeTaN and NiFe/IrMn/NiFe trilayer films,” J. Appl. Phys., vol. 91, p. 6899, (2002).
15. Yoo, H.J.; Tseng, S.-H.; Tsai, C.S, Electronic Components and Technology Conference, 2003. Proceedings.53rd Volume , Issue , May 27-30, (2003)
16. R.E. Camley and D.L. Mills. J. Appl. Phys. **82** (1997)
17. Ruo-Fan Jiang; Shams, N.N.; Rahman, M.T.; Chih-Huang Lai, Magnetics, IEEE Transactions on Volume 43, Issue 10, (2007)
18. D. J. Twisselman and R. D. McMichael, J. Appl. Phys., vol. 93, p. 6903, May 2003.
19. N A Morley, J. Phys.: Condens. Matter **16** 4121-4129 (2004)
20. A. M. Crawford, D. Gardner, S. X. Wang, IEEE Trans. Magn. 38, 3168 (2002).
21. C. Pettiford, A. Zeltser, SZ. D. Yoon, V. G. Harri, C. Vittoria, N. X. Sun. J. Appl. Phys 99, 08C901 (2006).
22. X. Liu, Sasaki and J. K. Furdyna, Physical Review B 67, 205204 (2003).
23. M. G. Blamire, M. Ali, C. W. Leung, C. H. Marrows, and B. J. Hickey, Phys. Rev. Lett. 98, 217202 (2007).
24. A. Hoffmann, J. W. Seo, M. R. Fitzsimmons, H. Siegwart, J. Fompeyrine, J.-P. Locquet, J. A. Dura, and C. F. Majkrzak, Phys. Rev. B 66, 220406 (2002).
25. Landau. L. D. , Lifshitz. E. M., *Phys. Z. Sowietunion* 8, 153 (1935)
26. M. Chrita, G. Robins, R. L. Stamps, R. Sooryakumar, M. E. Filipkowski, C. J.

Gutierrez, G. A. Prinz, Phys. Rev. B 58, 869 (1998).

27. J. J. Krebs, P. Lubitz, A. Chaiken, and G. A. Prinz, Phys. Rev. Lett. 63, 1645 (1989).
28. B.V. McGrath, R.E. Camley, Leonard Wee, Joo-Von Kim, and R.L. Stamps, J. Appl. Phys 87, 6430 (2006).
29. *V. K.* Arkad'ev, J. Russ. Phys.-Chem. Soc. 44, 165 (1912)
30. S. V. Vonsovskii, Ferromagnetic Resonance (Pergamon: Oxford, 1966).
31. J. H. E. Griffiths, Nature London 158, 670 1946
32. S. Chikazumi, Physics of Ferromagnetism (Oxford: New York, 1996).
33. A. J. R. Ives, J. A. C. Bland, R. J. Hicken, and C. Daboo, Phys. Rev. B 55, 12428 (1997).
34. Green, G. & Lloyd, J.T. Phil. Mag. 3, 321 (1970)
35. N.W. Ashcroft and N.D. Mermin, Solid-State Physics, (1976)
36. S. M. Rezende, A. Azevedo, and F. M. de Aguiar, Phys. Rev. B 66, 064109 ~2002!
37. J. J. Krebs, P. Lubitz, A. Chaiken, and G. A. Prinz, Phys. Rev. Lett. 63, 1645 (1989).
38. Charles Kittel, Introduction to Solid State Physics, (1953)
39. Salanskii and Mikhailovskii, JETP, Vol. 18, 9 (2006)
40. H. Puszkarski, Prog. Surf. Sci. 9, 191 (1979).
41. B.V. McGrath, R.E. Camley, Leonard Wee, Joo-Von Kim, and R.L. Stamps, J. Appl. Phys 87, 6430 (2006).
42. M. R. Freeman and J. F. Smyth., J. Appl. Phys. 79 , 5898 (1996).
43. C. Pettiford, J. Lou, L. Russell, N. X. Sun, Appl. Phys. Lett., 92, 122506 (2008).
44. N. X. Sun, S. Mehdizadeh, C. Bonhote, Q. F. Xiao, and B. York, J. Appl. Phys. 97, 10N904 (2005).

45. S. X. Wang, N. X. Sun, M. Yamaguchi & S. Yabukami , Nature, 407, 150, (2000).
46. N. X. Sun and S. X. Wang, IEEE Trans. Magn, 36, 2506 (2000).
47. Tsai, C. S.; Li, J. Y.; Chen, M. J.; Yu, C. C.; Liou, Y.; Hung, D. S.; Yao, Y. D Journal of. Magnetism and Magnetic Materials, 282, 57-60 (2004)
48. B. D. Cullity. Introduction to Magnetic Materials. (1972)
49. A. I. Shames, E. Rozenberg, W. H. McCarroll, M. Greenblatt, and G. Gorodetsky, Phys. Rev. B., 64, 172401 p.4 (2001).
50. Y. H. Ren, C.Wu, G.Yu, C. Pettiford, and N. X. Sun, Phys. Rev. B, submitted.
51. I A McIntyre, J. Phys. E: Sci. Instrum. 17 274-276
52. Victor David, Arnd Krueger, Philippe Feru, LASER FOCUS WORLD (2007)
53. Emily A. Gibson, David M. Gaudiosi, Henry C. Kapteyn, and Ralph Jimenez, OPTICS LETTERS, / Vol. 31, No. 22 (2006)
54. Patrick O'Shea, Mark Kimmel and Rick Trebino, J. Opt. B: Quantum Semiclass. Opt. 4 44-48 (2002)
55. J. H. Griffiths, J. Owen, J. G. Park, and M. F. Partridge, Phys. Rev. 108, 1345 (1957).
56. J. A. Sidles, J. L. Garbini, K. J. Bruland, D. Rugar, O. Züger, S. Hoen, and C. S. Yannoni , Rev. Mod. Phys. 67, 249 (1995).
57. M. D. Kaufmann, Magnetization dynamics in all-optical pump-probe experiments: spin-wave modes and spin-current damping, (2006)
58. Th. Gerrits, J. Hohlfeld, O. Gielkens, K. J. Veenstra, K. Bal, Th. Rasing, and H. A. M. vanden Berg. J. Appl. Phys., 89, 7648 (2001).
59. T. M. Crawford, T. J. Silva, C. W. Teplin, and C. T. Rogers, Appl. Phys. Lett., 74, 3386 (1999).

60. T. M. Crawford, C. T. Rogers, T. J. Silva, and Y. K. Kim, Appl. Phys. Lett., 68, 1573 (1996)
61. G. Meyer, A. Bauer, T. Crecelius, I. Mauch, and G. Kaindl, Phys. Rev. B 68, 212404 (2003)
62. T. D. Rossing, J. Appl. Phys. 34, 1133 (1963).
63. X. Liu, Y. Y. Zhou, and J. K. Furdyna, Phys. Rev. B 75, 195220 (2007)
64. C. E. Patton ,Classical theory of spin-wave dispersion for ferromagnetic metals (2005)
65. T. L. Kirk, O. Hellwig, and Eric E. Fullerton, Phys. Rev. B 65, 224426 (2002).
66. R. J. Hicken, A. Barman, V. V. Kruglyak, and S. Ladak, J. Phys. D: Appl. Phys. 36 2183 (2003).
67. Cheng Wu, Amish N. Khalfan, Carl Pettiford, Nian X. Sun, Steven Greenbaum, and Yuhang Ren *J. Appl. Phys.* 103, 07B525 (2008)
68. C. Pettiford, J. Lou, L. Russell, N. X. Sun , *Appl. Phys. Lett.*, 92, 122506 (2008).
69. B. Rameev, F. Yildiz, S. Kazan, B. Aktas, A. Gupta, L. R. Tagirov, D. Rata, D. Buergler, P. Grunberg, C. M. Schneider, S. Kammerer, G. Reiss, A. Hutten, Phys. Status Solidi A 203, 1503 (2006).
70. H. W. Xi, R. M. White, Phys. Rev. B 62, 3933 (2000).
71. S. M. Rezende, A. Azevedo, F. M. de Aguiar, J. R. Fermin, W. F. Egelhoff, and S. S. P. Parkin, Phys. Rev. B 66, 064109 (2002).
72. C. Pettiford, N. X. Sun. etc., unpublished.
73. P. E. Wigen, C. F. Kooi, M. R. Shanabarger, and T. D. Rossing, Phys. Rev. Lett. 9. 206 (1962).
74. J. F. Cohran, J. Appl. Phys. 70, 6545 (1991)

75. R W Teale and F Pelegrini, J. Phys. F: Met. Phys. 16 (1986)
76. D. M. Wang, Y. H. Ren, X. Liu, J. K. Furdyna, M. Grimsditch, R. Merlin. Phys. Rev. B 75, 233308 (2007).
77. C. Kittel, Phys. Rev. 110, 1295 (1958).
78. A. M. Closton, J. Phys. Chem. Solids. 1,129 (1956)
79. M. Sparks, Ferromagnetic Relaxation Theory (1964)
80. R. D.McMichael, J. Appl. Phys. 83, 7037 (1998)
81. B. Kunar. J. Appl. Phys. 93, 7723 (2003)
82. J. K. Miller, J. Qi, Y. Xu, Y.-J. Cho, X. Liu, J. K. Furdyna, I. Perakis, T. V. Shahbazyan, and N. Tolk, Phys. Rev. B 74, 113313 (2006)
83. M. Syperek, D. R. Yakovlev, A. Greilich, J. Misiewicz, M. Bayer, D. Reuter, and A. D. Wieck, Phys. Rev. Lett. 99, 187401 (2007)
84. L. Cheng, Material based control of ultra-fast relaxation of in ferromagnetic thin films, (2006)
85. M. van Kampen, Ultrafast spin dynamics in ferromagnetic metals, PhD thesis, Technische Universiteit Eindhoven, (2003).
86. B. Koopmans, M. G. Koerkamp, T. Rasing and H. van den Berg, Phys.Rev.Lett. 74, 3692 (1995).
87. M. van Kampen, C. Jozsa, J. T. Kohlhepp, P. LeClair, L. Lagae, W. J. M.de Jonge and B. Koopmans, All-optical probe of coherent spin waves, Phys.Rev. Lett. 88, 227201 (2002).
88. Z. Qiu and S. Bader, Surface magneto-optic Kerr effect (SMOKE), J.Magn. Magn. Mater 200, 664 (1999).

89. J. Hohlfeld, E. Matthias, R. Knorren and K. Bennemann, Phys. Rev. Lett. 78, 4861 (1997).
90. M. Lisowski, P. A. Loukakos, A. Melnikov, I. Radu, L. Ungureanu, M. Wolf and U. Bowensiepen, Phys. Rev. Lett. 95, 137402 (2005).
91. Z. Qiu and S. Bader, Surface magneto-optic Kerr effect (SMOKE), J. Magn. Magn. Mater 200, 664 (1999).
92. T. G. Castner, Jr. and Mohindar S. Seehra, Phys. Rev. B 4, 38 - 45 (1971)
93. A. I. Shames, E. Rozenberg, W. H. McCarroll, Phys. Rev. B 64, 172401 (1993)
94. C. H. Back, D. Weller, J. Heidmann, D. Mauri, D. Guarisco, E. L. Garwin and H. C. Siegmann, Magnetization reversal in ultrashort magnetic field pulses, Phys. Rev. Lett. 81, 3251 (1998).
95. Laurence D. Barron, Pure & App!. Chem., Vol. 57, No. 2, pp. 215—223, (1985).
96. C. H. Back, D. Weller, J. Heidmann, D. Mauri, D. Guarisco, E. L. Garwin and H. C. Siegmann, Phys. Rev. Lett. 81, 3251 (1998).
97. M. Djordjevic, G. Eilers, A. Parge, M. M¨unzenberg and J. S. Moodera, Jour. Appl. Phys. 99, 08F308 (2006).
98. J. Sandercock, Light scattering in solids III, Springer Verlag, Berlin, Heildelberg, New York, (1982).
99. C.-Y. You and S.-C. Shin, Jour. Appl. Phys 84, 541 (1998).
100. M. Fahnle and D. Steiauf, Dissipative magnetization dynamics close to the adiabatic regime, Private correspondence (2006).
101. M. Fahnle, Nanosecond relaxation processes, 1133 (2005)
102. V. Kambersky, , Can. Jour. Phys. 48, 2906 (1970).

103. L. Guidoni, E. Beaurepaire and J. Y. Bigot, Magneto-optics in the ultrafast regime: thermalization of spin populations in ferromagnetic films, Phys. Rev. Lett. 89, 017401 (2002).
104. E. Beaurepaire, J.-C. Merle, A. Daunois and J.-Y. Bigot, Ultrafast spin dynamics in ferromagnetic nickel, Phys. Rev. Lett 76, 4250 (1996).
105. P. Landeros, Rodrigo E. Arias, and D. L. Mills, Phys. Rev. B 77, 214405 (2008),
106. M. van Kampen, C. Jozsa, J. T. Kohlhepp, P. LeClair, L. Lagae, W. J. M.de Jonge and B. Koopmans, Phys. Rev. Lett. 88, 227201 (2002).
107. S. M. Rezende, Phys. Rev. B 31, 570 - 573 (1985)
108. D. M. Wang, Y. H. Ren, X. Liu, J. K. Furdyna, M. Grimsditch, and R. Merlin, Phys. Rev. B 75, 233308 (2007).
109. D. Shaltiel, W. Low, Phys. Rev. 124, 1062 - 1067 (1961)